To the Graduate Council:

I am submitting herewith a thesis written by Christopher James Heiny entitled "Joint Size Estimation Using Joint Traces on Borehole Walls." I have examined the final electronic copy of this thesis for form and content and recommend that it be accepted in partial fulfillment of the requirements for the degree of Master of Science in Geology.

William M. Dunne
Major Professor

I have read this thesis and
Recommend its acceptance:

Matthew Mauldon

Robert D. Hatcher, Jr

Edmund Perfect

Accepted for the Council

Anne Mayhew

Vice Provost and
Dean of the Graduate Studies

(Original signatures are on file with official student records.)

JOINT SIZE ESTIMATION USING JOINT TRACES ON BOREHOLE WALLS

A Thesis
Presented for the
Master of Science Degree
The University of Tennessee, Knoxville

Christopher James Heiny
December 2004

ACKNOWLEDGMENTS

First, I would like to thank the National Science Foundation, the Geological Society of America, and the Society of Professional Well Log Analysts for their financial assistance with this project. Also I would like to thank a particular petroleum company, whom has asked to remain unnamed, for supplying the FMI logs and assisting me in the field. This project would not have been possible without the assistance from the above organizations/companies.

Secondly, I would like to thank my thesis advisor, Dr. William Dunne, for his guidance and knowledge in this project. Although there were times when I thought he was a little hard on me, I feel that my graduate experience has better equipped me for a professional geology career. Also, I would like to thank Dr. Matthew Mauldon, the co-chair on this project. This project would not have gotten off the ground without his insight early on. I would also like to thank my other thesis committee members, Dr. Edmund Perfect and Dr. Robert D. Hatcher, for both their insight in this project and their valued instruction in classes. And I would also like to thank the professors that I have received instruction from, both at the graduate and undergraduate level (which covers most of the department). I feel that the knowledge that I have gained from these professors has really prepared me for the future.

Third, I would like to thank Xiaohai Wang, Dr. Mauldon's PhD student at Virginia Tech, for the creation of the fracture simulation program and his valued assistance in the estimators.

And lastly, I would like to thank my fiancée, Meredith, and my family for supporting and helping me. Without you all, this degree would not be possible.

ABSTRACT

One approach to characterizing subsurface joint populations is to assume surface joint patterns are representative of joints at depth. Yet, many times, either the analogous surface joints are unexposed, or absent because surface rocks did not experience the same deformation history. The alternative of direct subsurface characterization has been limited by joints not being resolvable in seismic data and borehole data not yielding fracture size. The present approach uses the subsurface geometry of joint/borehole intersections to estimate mean joint size (mean joint length and width) and aspect ratio (joint length to width ratio), and presents a new method for determining the volumetric joint intensity as estimated with cycloidal scanline samples.

This study focused on bed-normal joints in sedimentary rocks that typically terminate at bedding surfaces, have bed-parallel lengths greater than or equal to the bed-perpendicular lengths, and are rectangular. Rectangular joint/borehole intersections have six geometries: complete, long-edge, short-edge, corner, end, and pierced, which are differentiated by completeness of borehole intersection and joint trace position on the borehole wall as a function of borehole and joint orientation. The counts for the intersection geometries are used to estimate mean joint size and aspect ratio.

The approach yielded accurate mean size estimates for synthetic trace populations. Based on this success, the estimators were applied to borehole joint populations from FMI (Formation MicroImager) data logs in the Mesaverde Group of

the Piceance Basin, Colorado. Subsurface estimates yielded bed-parallel and perpendicular lengths greater than for exposed joints along the basin perimeter, but the surface and subsurface shared small aspect ratios of ~1:1. The difference in estimated size may reflect differences in deformation history between the basin center and perimeter.

TABLE OF CONTENTS

Chapter		Page
I.	**INTRODUCTION**	1
	Study Area	3
	Depositional and Tectonic Basin History	6
	Timing of Joint Formation	9
II.	**SURFACE FRACTURE ANALYSIS**	11
	Data Collection	11
	Results	14
III.	**BOREHOLE-BASED ESTIMATORS FOR JOINT SIZE**	24
	Formation MicroImager Tool and Well Logs	24
	Joint Shape Assumption	30
	Borehole-Bedding-Joint Geometry	32
	Joint/Borehole Intersection Geometries	32
	Complete (A) Intersections	35
	Pierced (C) Intersections	40
	Edge (B) Intersections	41
	B_1 Intersections	41
	B_2 Intersections	42
	B_3 Intersections	42
	B_4 Intersections	43
	Joint Size Estimators	44
	Case 1	44
	Case 2	50
	Case 3	52
IV.	**SIMULATION RESULTS**	55
	Case 1	55
	Case 2	59
V.	**SUBSURFACE JOINT ANALYSIS**	62
	Joint Orientations	62
	Joints by Formation	64
	Joints by Lithology	64
VI.	**DISCUSSION**	73
	Comparison of Subsurface and Surface Mean Size Estimates	73
	Joint Enhancement	73
	Misidentification of Joint Traces/Intersections	76

TABLE OF CONTENTS…continued

Chapter Page

VII. **CONCLUSIONS** 80

REFERENCES CITED 81

APPENDICES 89
Appendix A: Case 1 Estimator Derivation 90
Appendix B: Case 3 Estimator Derivation 98
Appendix C: P_{32} Determination from Cycloidal Scanlines and Data from the Mesaverde Group, Piceance Basin, CO 108
VITA 117

LIST OF TABLES

Table		Page
1.	Surface dip deviation data for Figure 11	19
2.	Summary of straight scanline data for exposed fractures within the Mesaverde Group, Piceance basin, Colorado	21
3.	Circular scanline data for exposed fractures within the Mesaverde Group, Piceance basin, Colorado	22
4.	Joint/Borehole intersection definitions and characteristics	39
5.	Case 1 simulation data along with length and width estimates to accompany Figure 28	58
6.	Case 2 simulation data	61
7.	Intersection data and size estimates of subsurface fractures by stratigraphy	67
8.	Intersection data and size estimates of subsurface fractures by lithology	70
9.	Percentage of subsurface joints occurring in single vs. mixed lithologies, or with borehole heights greater than 10 ft (~3 m)	74
C-1.	Summary of P_{32} estimates by formation for each well	113
C-2.	Summary of P_{32} estimates by lithology for each well	115

LIST OF FIGURES

Figure		Page
1.	General geology and geography of the Piceance basin, CO	4
2.	Generalized cross section of the Piceance basin	5
3.	Visualization of the paleogeography of the western United States during the Late Cretaceous	7
4.	Timeline of depositional and geologic events as they relate to Upper Cretaceous to Lower Tertiary stratigraphy	8
5.	Surface joint sampling localities and joint orientation plots	12
6.	Joint analysis using a straight scanline at the Campbell pavement, northern Piceance Basin, CO	13
7.	Exposure of vertically bedded sandstone in the Mesaverde Group at Rifle Gap, CO	15
8.	Wyatt pavement joint trace map	16
9.	Photograph and fracture trace map of the Meeker pavement	17
10.	Circular scanline/window of radius R	18
11.	Plot of fracture dip deviation from normal to bedding for surface fractures	19
12.	High intensity fractures located near the Wyatt outcrop locality	23
13.	Location of the Piceance Creek gas field where the six sample wells are located	25
14.	The Formation MicroImager tool	26
15.	Example FMI Log showing different fracture intersection types and also other well log data	27
16.	Examples of planar structure (i.e. fracture, bedding, etc.)/borehole intersections where the plane is perpendicular to the borehole axis, and inclined to the borehole axis	29
17.	Block diagram showing typical bed-normal joint shapes in sedimentary rocks	31
18.	Complete, edge, and piercing joint/borehole intersections for the case of joints normal to the borehole axis	33
19.	Plan view of borehole intersection types for a borehole-normal joint	35
20.	Geometry of a joint inclined to the borehole axis and the corresponding projected joint	36
21.	Loci of centers of boreholes with different intersection types on a rectangular joint projected onto a plane normal to the borehole axis where D<W	37
22.	Loci of centers of boreholes with different intersection types on a rectangular joint projected onto a plane normal to the borehole axis where D>W	38
23.	Rock mass (cube) containing identical, parallel, rectangular joints penetrated by a borehole of diameter D	45

LIST OF FIGURES…continued

Figure		Page
24.	Projected joints within rock mass of Figure 23	46
25.	Corresponding intersection areas for the projected joints in Figure 24	47
26.	Width determination from a C intersection	51
27.	Graphical interface for the joint simulation program	56
28.	Estimator performance for Case 1 simulations	57
29.	Estimator performance for Case 2 simulations	60
30.	Equal-area stereonet plots of joint poles to bedding in all of the wells	63
31.	Plot of fracture dip deviation from normal to bedding for the subsurface fractures	65
32.	Equal-area stereonet plots showing all joints with dip greater than 65^0	66
33.	Graph of dip azimuth vs. depth for Well 3	77
34.	Picture of a core showing the joint linkage	78
B-1.	Illustration of the pdf's of the L and W' of the fractures	100
C-1.	Generation and dimensions of a cycloidal scanline	110
C-2.	Cycloidal scanline deployment example	112

I. INTRODUCTION

The purpose of this thesis is to characterize subsurface joint size, where joint length is parallel to bedding and width is perpendicular to bedding, using a cylindrical sampling geometry, such as a borehole. Joint characteristics influence fluid behavior during hydrocarbon migration and accumulation, plus play a major role in governing rock mass stability such as in tunnels, highway cuts, mines, foundations, and other excavated rock masses. For example, joint intensity, density, orientation, and size influence connectivity of joint networks, greatly affecting the rock mass permeability (Witherspoon et al., 1979; Thorp et al., 1983; Barton, 1995; Becker and Gross, 1996; Odling, 1997). Alternatively, joints are structural discontinuities that can slip, reducing the rock strength of rock slopes, tunnels, and foundations (Amadei and Savage, 1993; Barton et al., 1993). As a result, fracture-flow models, block models for rock engineering, and analytical analyses of rock mass stability incorporate several joint characteristics, like aperture, orientation, spacing, intensity, density, size, and roughness, as input parameters (LaPointe and Hudson, 1985; Cacas et al., 1989).

For surface joint characterization, joint data are collected along straight or circular scanlines (Priest & Hudson, 1981; LaPointe and Hudson, 1985; Becker and Gross, 1996; Mauldon 1998; Mauldon et al., 1999; Mauldon et al., 2001; Rohrbaugh et al., 2002), and/or are mapped and tabulated on a fracture pavement (Dershowitz and Einstein, 1988; Wu and Pollard, 1995). Procedures are available for this suite of techniques with sufficient rock exposure, to obtain unbiased estimates of joint characteristics such as mean size, density, intensity, and aperture.

When attempting to characterize joint size from subsurface data, two strategies may be used: extrapolating surface characteristics into the subsurface or estimating characteristics directly from the subsurface. Even where surface data about a joint system are of high quality and from the same stratigraphic unit, which is not always possible, these data may only have limited utility in the subsurface because of differences in the loading histories for fracture generation between the surface and subsurface locations of the stratigraphic unit (Engelder, 1987; Engelder and Fischer, 1996). For example, subsurface rocks undergo less unloading and hence less thermoelastic contraction, and typically less joint generation (Engelder, 1985; Engelder, 1987; Engelder and Fischer, 1996). Another potential difference in loading history is the timing of fluid pressure events, particularly related to hydrocarbon migration and accumulation. Also, in the case of a basin, the basin-rim rocks may undergo a different burial history as compared to the basin-center rocks, and thus experience different pressures and temperatures associated with burial and hydrocarbon generation (Law, 2002; Yurewicz et al., 2003).

Given the potential differences in joint-forming loading histories between the surface and subsurface, the ideal strategy for characterizing a subsurface joint system is to use subsurface data. For example, the U.S. Department of Energy Multiwell Experiment (MWX) project in the east-central Piceance basin, Colorado, characterized subsurface joint orientation, distribution, morphology, mineralization, and fluid inclusions to derive a synthesis of tectonic events in the basin (Finely and Lorenz, 1989; Lorenz and Finely, 1991; Lorenz and Hill, 1994). Additionally, information

about the average joint height and frequency within the MWX well-bores was used to estimate the average subsurface joint spacing (Narr, 1996).

Here, I am following the second strategy and using subsurface joints that intersect boreholes in sedimentary rocks to directly estimate mean joint length and width, assuming a rectangular fracture shape. This method characterizes the types of fracture/borehole intersection, and then uses the different intersection counts to estimate mean length and width. For this analysis, new estimators were developed and tested using a fracture simulator (Wang, personal communication), where all fracture parameters are known. These estimators were then applied to subsurface joints in the Mesaverde Group, in the Piceance basin, Colorado.

Study Area

Surface and subsurface fracture data were collected from the Piceance basin in western Colorado (Figure 1). The basin is bound to the east by the Grand Hogback monocline and the White River uplift, to the south by the Uncompahgre uplift, to the north by the Uinta Mountains, and to the west by the Douglas Creek arch (Figure 1). Along the basin edges, the Upper Cretaceous to Lower Tertiary Mesaverde Group, Paleocene Ohio Creek Formation, and the Eocene Wasatch Formation are exposed. These units dip steeply to moderately into the basin at the rim and are capped by the younger Eocene Green River and Uinta Formations (Figure 2).

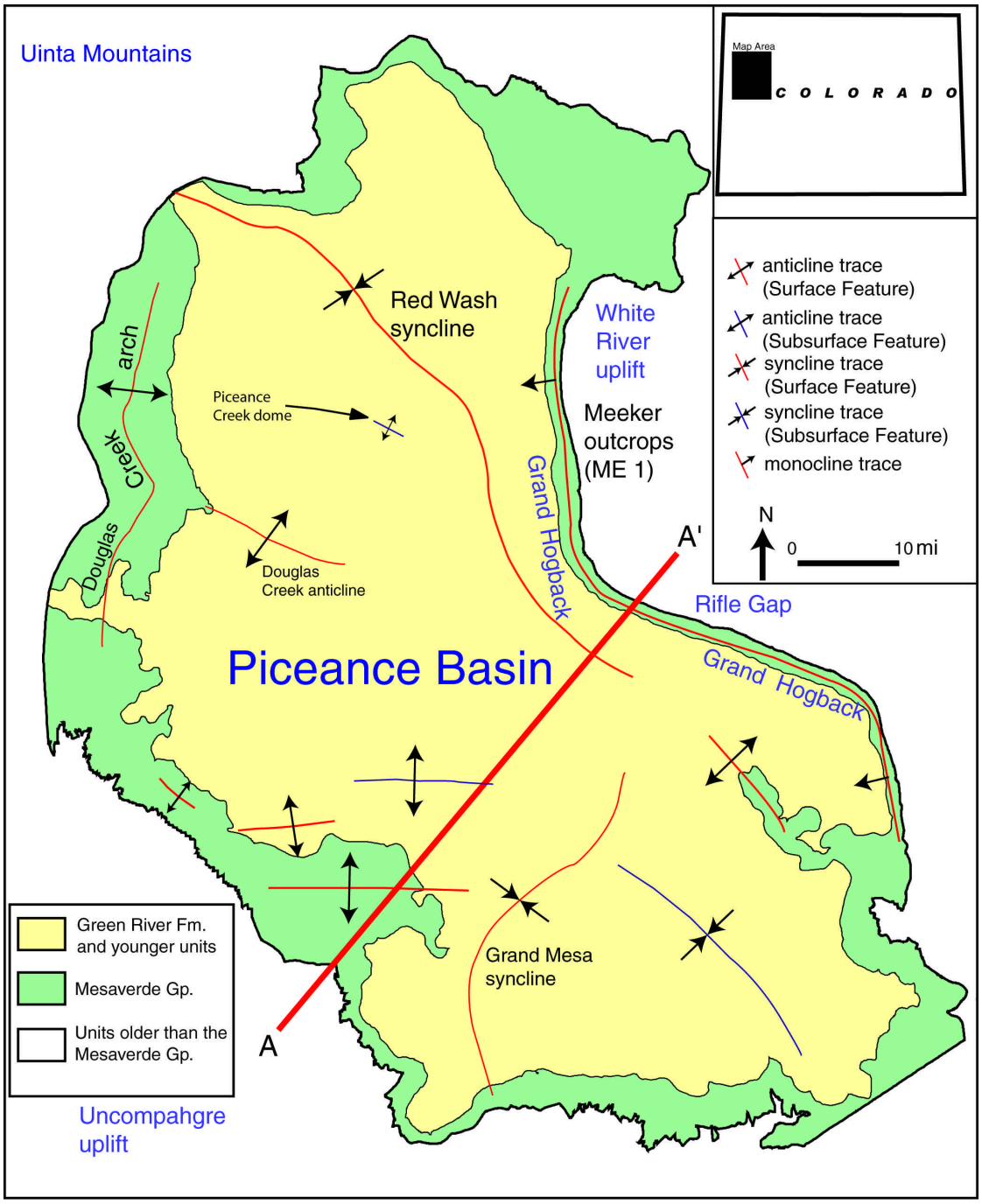


Figure 1. General geology and geography of the Piceance basin, Colorado (Modified from Patterson et al., 2003). The generalized cross-section A-A' is shown in Figure 2.

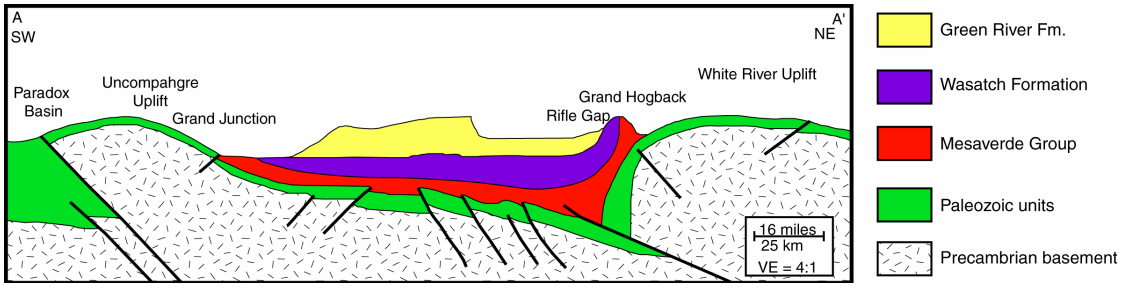


Figure 2. Generalized cross section of the Piceance Basin. Cross section is along A-A' in Figure 1 and shows stratigraphic and structural geometries. (Modified from Wilson et al., 2003.)

Depositional and Tectonic Basin History

The history of the Piceance basin begins during the waning Sevier orogeny (Johnson, 1992), when an E-W-directed tectonic compression created highlands in Nevada and western Utah during the Early to Middle Cretaceous (Johnson, 1992; Carroll, 2003). These highlands provided sediment that was transported eastward by rivers and deposited into and along the Cretaceous western interior seaway (Figure 3) during the late Early Cretaceous (Franczyk et al., 1992; Johnson, 1992; Cumella et al., 2003; Patterson et al., 2003). The coarsening-upward successions of cross-bedded sandstones interbedded with marine shales of the Castlegate, Sego and Lower Iles Formations in the lowermost Mesaverde Group, preserve a prograding-shoreline sequence (Figure 4) (Johnson, 1992; Patterson et al., 2003).

The western Sevier highlands continued as the main sediment source for the basin in the early Middle Cretaceous (Johnson, 1992; Carroll, 2003). During this time, the Western Interior Seaway shoreline regressed, leading to deposition of the thick, cross-bedded marine shoreface sandstones of the Rollins Sandstone (Upper Iles Formation) and the coastal plain deposits of the middle Iles and lower Williams Fork Formations consisting of fine-grained, meandering stream sediments along with coals deposited in adjacent swamps (Johnson, 1992; Cumella and Ostby, 2003). Continued regression created a broad alluvial plain that received sediment via braided streams (Johnson, 1992; Cumella and Ostby, 2003; Patterson et al., 2003), leading to deposition of the middle Williams Fork Formation with shales and interbedded sandstone with trough to low angle cross-beds and numerous erosional surfaces.

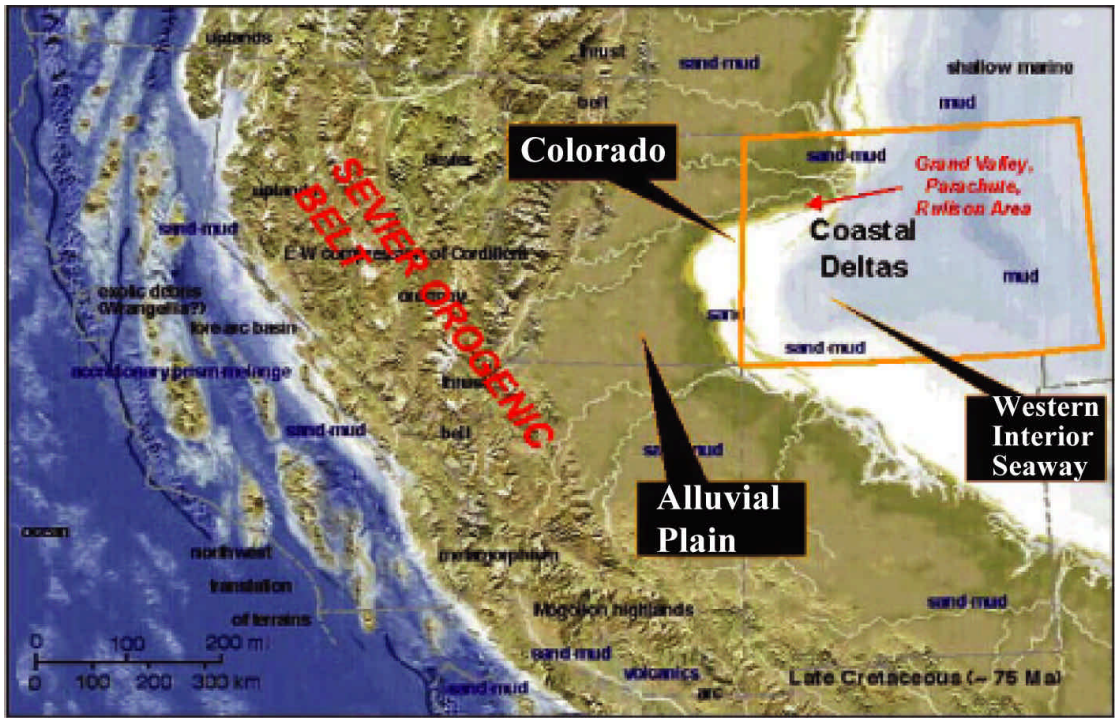


Figure 3. Visualization of the paleogeography of the western United States during the Late Cretaceous (~75 million years ago). Colorado (outlined in orange) was mostly submerged in the western interior seaway. Sediment derived from the Sevier orogenic belt accumulated in the seaway although Laramide uplifts triggered a gradual retreat of this seaway. (Modified from Cumella and Ostby, 2003.)

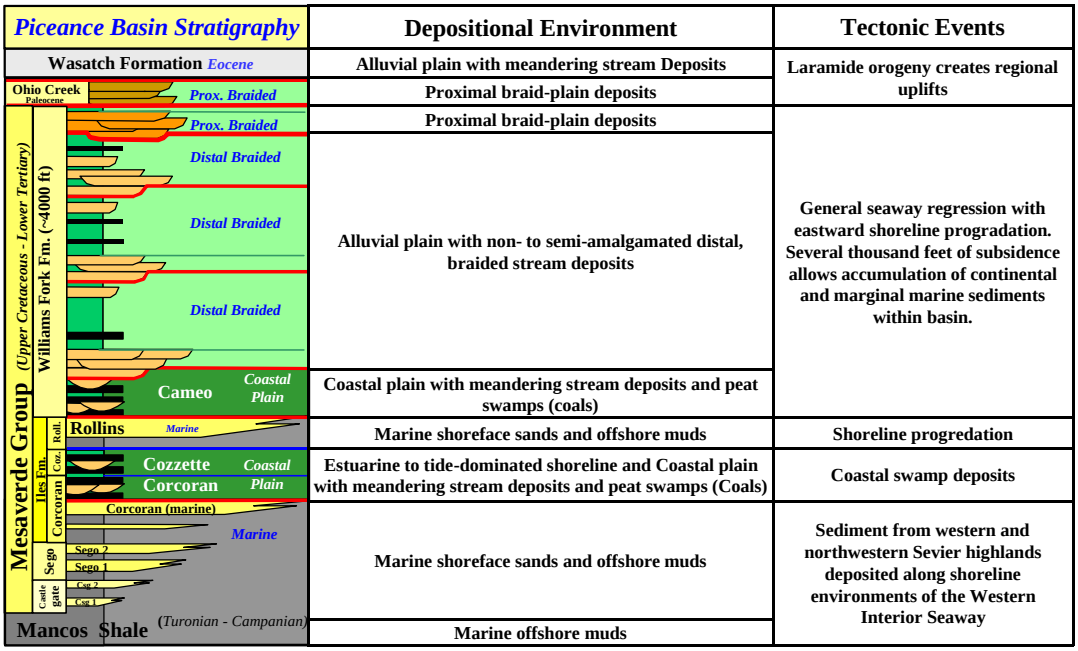


Figure 4. Timeline of depositional and geologic events as they relate to Upper Cretaceous to Lower Tertiary stratigraphy (modified from Patterson et al., 2003).

As deposition continued, the Laramide orogeny initiated with a maximum horizontal compression trending approximately E-W (Brown et al., 1986; Johnson, 1992; Verbeek and Grout, 1998; Carroll, 2003; Cumella and Ostby, 2003; Johnson and Flores, 2003; Patterson et al., 2003). The orogeny produced basement-cored structures, such as the Sawatch, Uncompahgre, and White River uplifts, the Douglas Creek arch, and the Grand Hogback monocline that collectively define the border of the Piceance basin (Johnson, 1992; Johnson and Flores, 2003). During this time, sedimentation shifted from the distal source of the Sevier highlands to the more proximal uplifts. Deposition initially occurred in amalgamated braided streams (early Laramide) and then in meandering streams as the alluvial plain broadened (Johnson and Flores, 2003). Therefore, the uppermost Williams Fork Formation, Ohio Creek Formation, and the Wasatch Formation all contain coarser-grained, thickly bedded sandstone packages with some locally-developed conglomerates (Patterson et al., 2003).

Timing of Joint Formation

The oldest joints, which are WNW to W-trending and bed-normal, are present in the Mesaverde Group and Wasatch Formation, but not in younger units, which implies that these master joints formed in response to a Laramide-controlled stress field (Grout and Verbeek, 1992; Verbeek and Grout, 1998). The Sevier-controlled stress regime had a similar geometry of principal stresses as the Laramide stress field, but is discounted as a source of driving stress because the deformation was quiescent

in the vicinity of the basin by the time of deposition of the lowermost Mesaverde Group (Brown et al., 1986; Johnson, 1992; Cumella and Ostby, 2003; Johnson and Flores, 2003). A younger joint set that terminates at the master joints in surface rocks is absent in subsurface rocks, which is interpreted to imply that these joints are related to stress-release during uplift at the basin rim (Finely and Lorenz 1989; Lorenz and Finely 1991; Lorenz and Hill 1994; Verbeek and Grout, 1998; and this study). As the oldest joint set is in both the surface and subsurface rocks, this master set is the focus of the study.

II. SURFACE FRACTURE ANALYSIS

Exposures of the Mesaverde Group were sampled around the Piceance basin perimeter at the Little Book Cliffs (LB), White River (WR), Campbell pavement (CP) adjacent to the White River, and Meeker (ME) (Figure 5). Joint geometries at Rifle Gap were found to reflect the surface slopes of the gap, indicating a surficially related modification of the fracture system, so these joints are not included in the present analysis.

Data Collection

At each sampling location, straight or circular scanlines and/or fracture maps were used to collect data regarding mean fracture size, density, and intensity, where density is defined as the as the number of joint centers per unit volume, and intensity is defined as fracture area per unit volume of rock mass (Rohrbaugh et al., 2002). For the straight scanline method, a straight sampling line is positioned along a bedding surface or profile, and the joint spacing, joint orientation, and if available, the apparent joint tracelength along bedding and/or joint height are noted for each joint intersected by the scanline (Figure 6). This technique was applied where only narrow pavements or rock formations are available, and typically contain doubly censored joints with no exposed trace tips, such as at Book Cliffs, White River, Meeker, and Campbell sites (Figure 5). Double censoring was caused by pavement terminations, loose material or foliage on bedding surfaces, by the poor exposure of the underlying unit (typically a

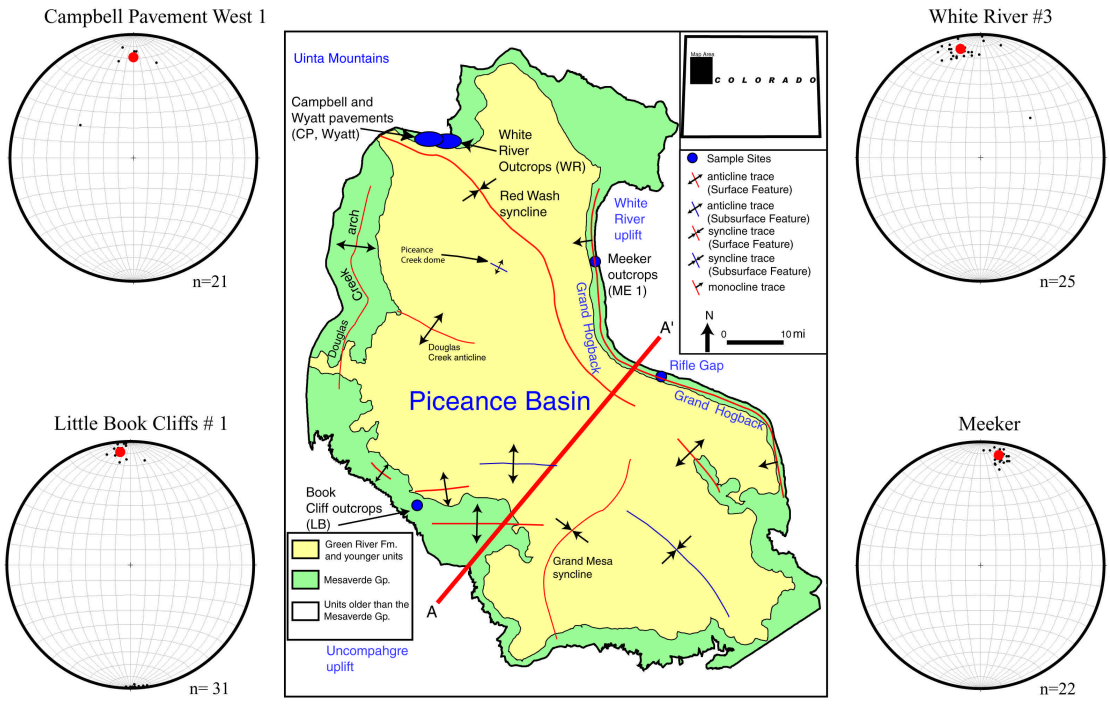


Figure 5. Surface joint sampling localities and joint orientation plots. Equal-area steronet plots of joint poles to bedding with bedding restored to the horizontal. Plots show individual joint orientations (black dots) and vector mean joint orientations (red dots). Blue dots on the map are sampling localities. Geologic map modified from Patterson et al., 2003.

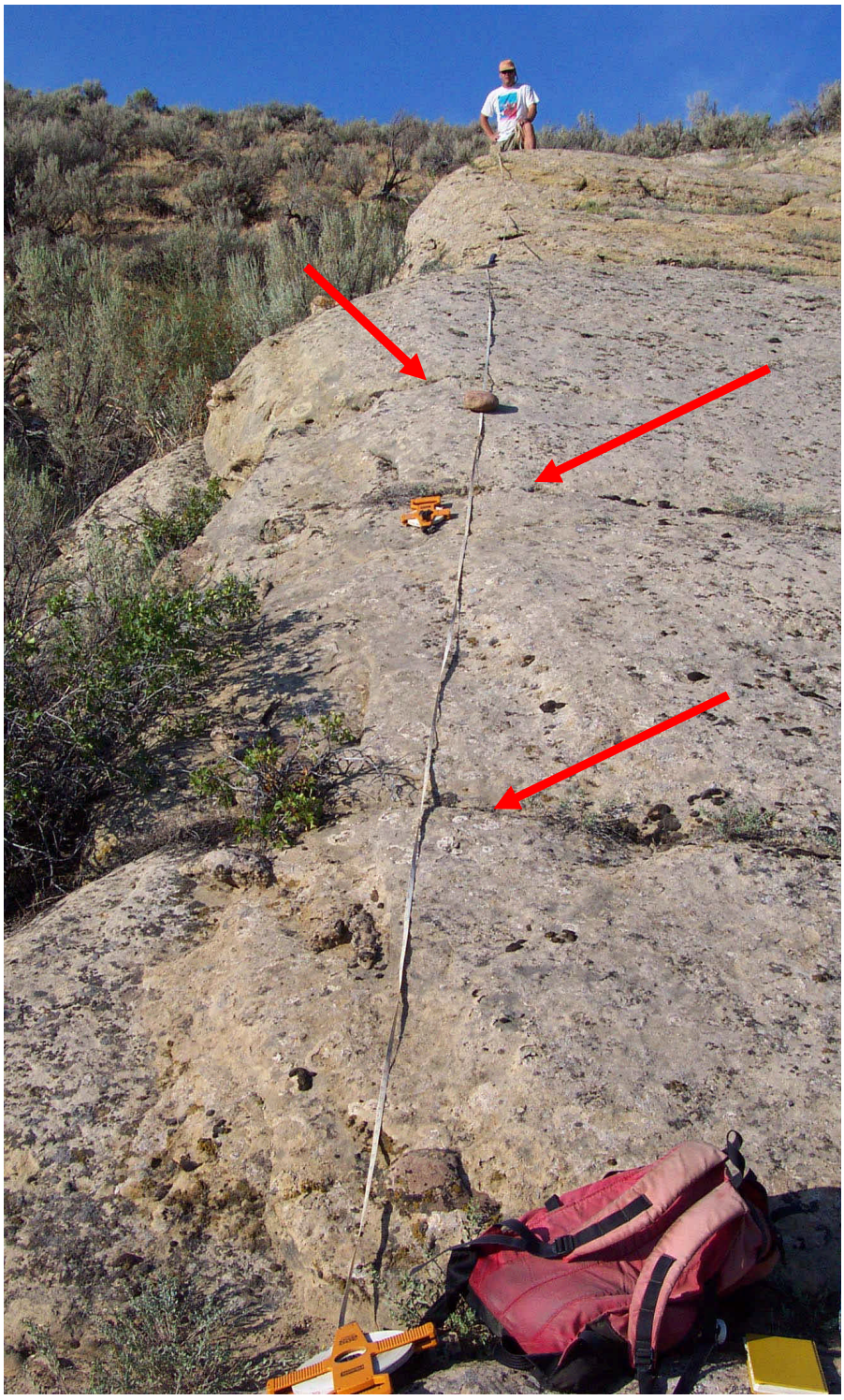


Figure 6. Joint analysis using a straight scanline at the Campbell pavement, northern Piceance basin, CO. The red arrows point towards sampled fractures along the scanline.

shale), or the absence of the overlying unit due to erosion for profiles. Joints terminate at exposed bedding surfaces where a lithologic contrast is present or absent (Figure 7).

Joint trace maps were completed for the well-exposed pavements that could be either efficiently hand mapped (Figure 8), or photographed and then digitally mapped using a computer drawing program (Figure 9), such as the Meeker, Wyatt, and Campbell localities. Once mapped, the joints were analyzed using circular scanlines. This method estimates mean tracelength, density, and intensity by randomly deploying circular sampling areas onto a rock pavement or outcrop, and only requires counts of the number of trace-circle intersections and/or counts of the number of trace terminations within circular area to determine the estimates (Figure 10) (Mauldon 1998; Mauldon et al., 1999; Mauldon et al., 2001; Rohrbaugh et al., 2002). This method is very time efficient and, unlike samples from the straight scanlines or area method, automatically corrects for biases related to orientation, censoring, and length (Mauldon et al., 2001; Rohrbaugh et al., 2002).

Results

Joints exposed at the four localities (Figure 5) were evaluated for orientation, mean bed-parallel lengths, and mean penetration depths or bed-perpendicular lengths, which are analogous to joint height or width (Pollard and Aydin, 1988). The master joint set strikes within 10° of an E-W trend (Figure 5), on average. Additionally, the surface joints are typically near bed-normal with less than 20° deviation from the normal to bedding, and in most cases, less than 10° (Figure 11, Table 1).



Figure 7. Exposure of vertically bedded sandstone in the Mesaverde Group at Rifle Gap, CO. Red arrows show joints that terminate at bedding surface, which is typical for these oldest bed-normal master joints. Person for scale.

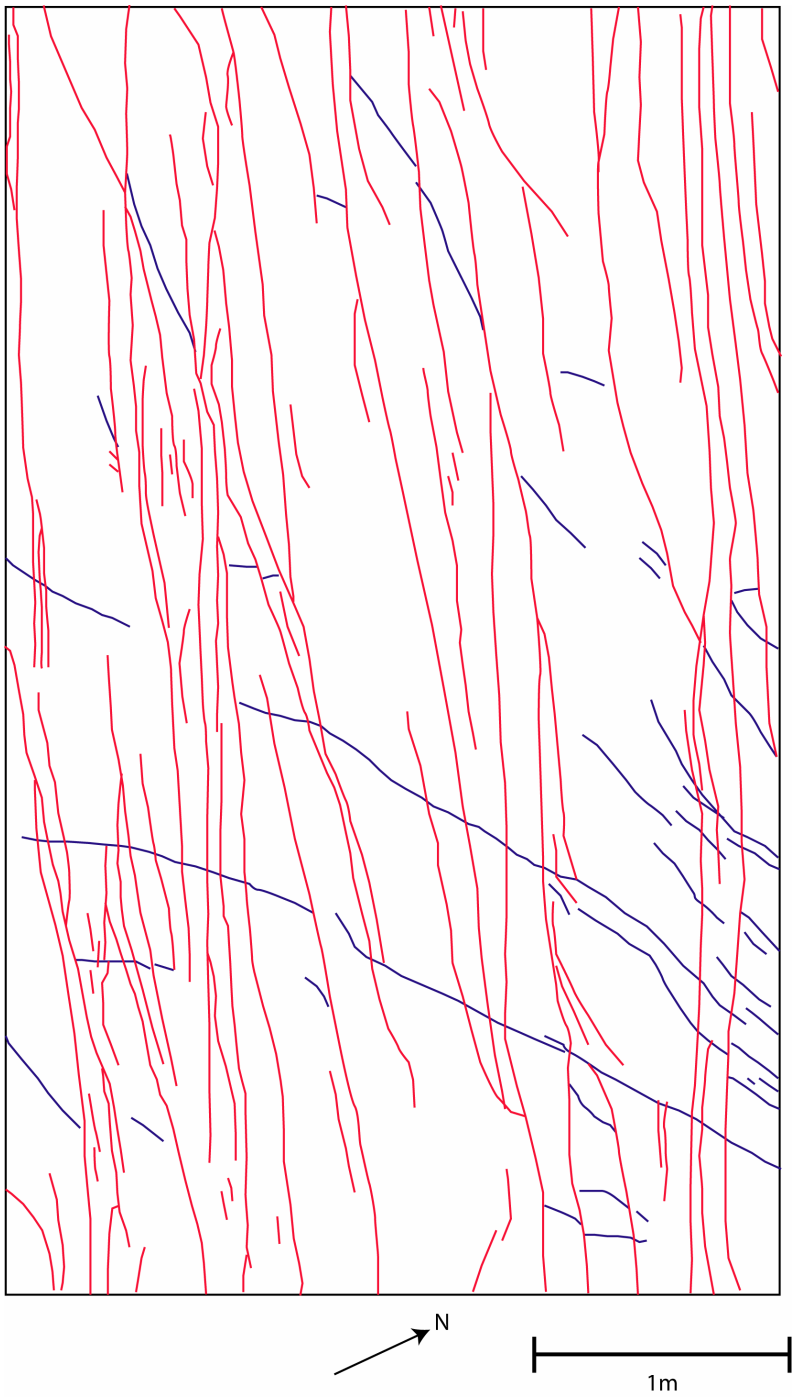


Figure 8. Wyatt pavement joint trace map. This pavement is of a sandstone unit within the Mesaverde Group located along the White River near the northern edge of the Piceance basin. The red traces outline the master joint set and the blue outline the cross set.

A



B

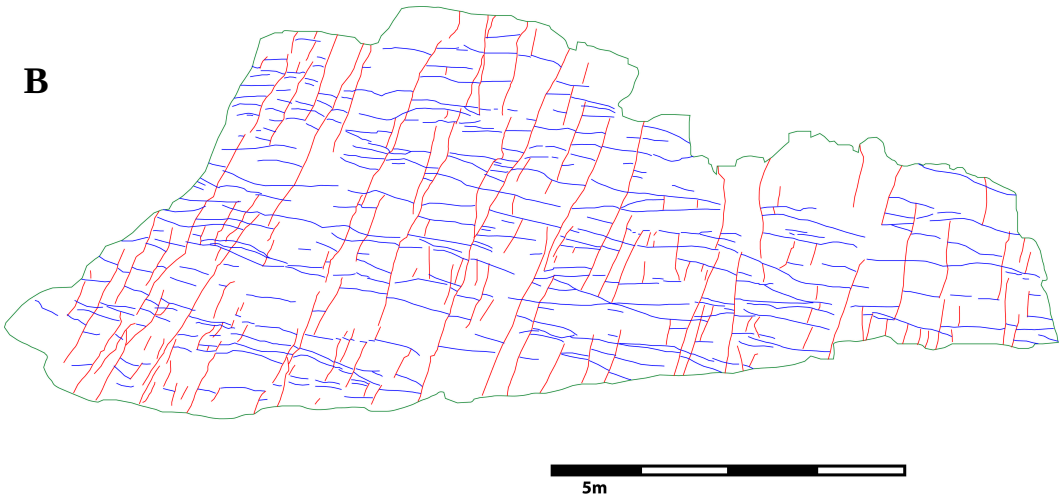


Figure 9. Photograph (A) and fracture trace map (B) of the Meeker pavement (ME1 on east side of Figure 6). The red traces are the master joint set and the blue are the cross joints.

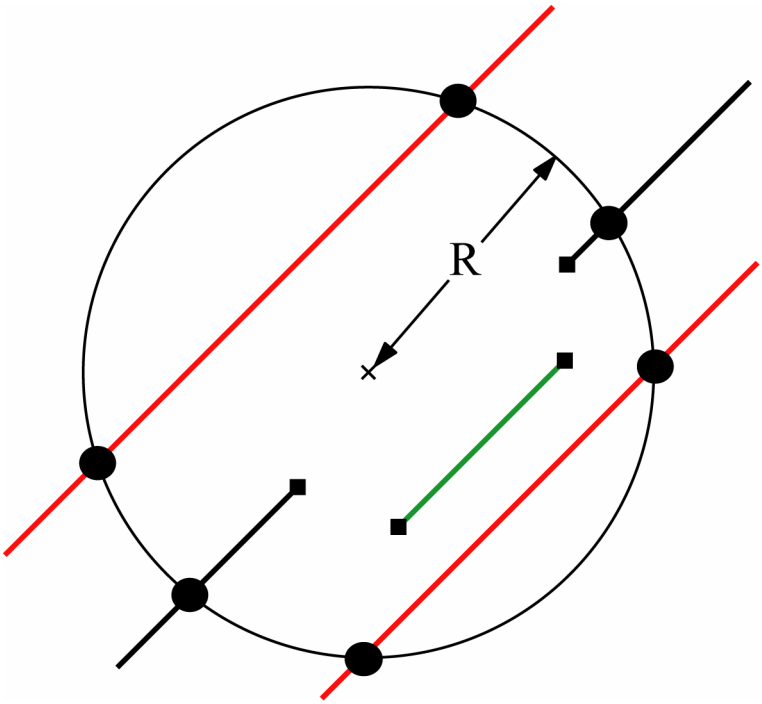


Figure 10. Circular scanline/window of radius R. Red traces completely transect the window, green traces are completely contained within the window, and black traces are partially contained in the window. The black dots represent scanline/fracture trace intersections and the squares represent joint terminations.

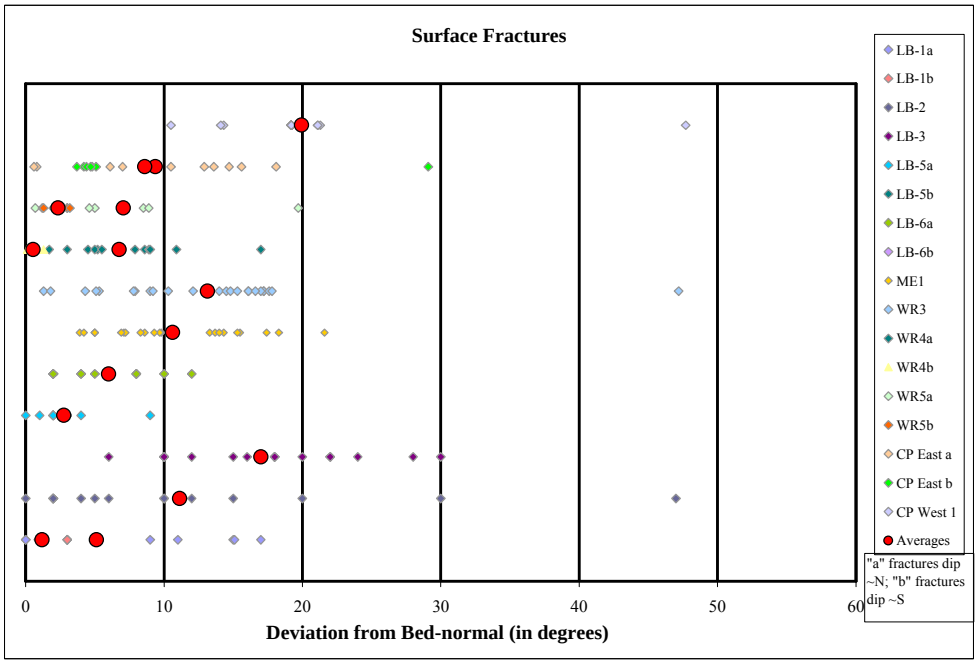


Figure 11. Plot of fracture dip deviation from normal to bedding for surface fractures. A bed-normal joint (dipping 90°) will plot as 0° on this graph. LB is the Book Cliffs outcrops, WR is the White River outcrops, ME is the Meeker outcrop, and CP refers to the Campbell pavement.

Table 1. Surface dip deviation data for Figure 11.

	Number Sampled	Mean	Median	Mode	Std Dev
LB1a	20	5.1	3	1	5.4
LB1b	11	1.2	1	1	0.6
LB2	15	11.1	6	2	12.9
LB3	17	17.0	18	10	6.8
LB5a	12	2.8	2	2	2.2
LB5b	2	3.0	3	n/a	n/a
LB6a	23	6.0	6	8	3.3
LB6b	1	6.0	6	n/a	n/a
ME1	22	10.6	9.5	5	5.1
WR3	25	13.2	14	17.2	8.8
WR4a	14	6.8	6.2	n/a	4.2
WR4b	3	0.5	0.2	n/a	0.7
WR5a	8	7.1	6.05	n/a	5.9
WR5b	5	2.3	3	3	1.0
CP East a	15	9.4	9.2	8.7	5.1
CP East b	7	8.6	4.7	n/a	9.2
CP West 1	2	19.9	19.2	19.2	6.8

The censored mean bed-parallel lengths from straight scanlines were measured at two localities, ME1 and WR3, and ranged from 1.2 m (3.9 ft) to 1.5 m (4.9 ft), respectively (Table 2). The apparent bed-perpendicular lengths from straight scanlines were measured at several localities and range from 0.9 m (3.0 ft) to 3.2 m (10.3 ft) (Table 2). Bed-parallel lengths from circular scanlines range from 1.6 m (5.2 ft) to 3.5 m (11.6 ft) (Table 3). Therefore, these estimates obtained from both methods for the bed-parallel and perpendicular tracelengths indicate that for the rectangular exposed joints, aspect ratios (L/W) are small and may even be 1:1 (Tables 2 and 3).

Linear intensity estimates from straight scanlines range from 0.7 m^{-1} (0.2 ft^{-1}) to 4.9 m^{-1} (1.5 ft^{-1}) (Table 2) and intensity and density estimates from circular scanlines range from 0.1 m^{-2} (0.01 ft^{-1}) to 4.6 m^{-2} (0.4 ft^{-2}), and 0.2 m^{-1} (0.06 ft^{-1}) to 7.2 m^{-1} (2.2 ft^{-1}) (Table 3). The larger density and intensity values from the CP West 1 and Wyatt localities are likely fault related. At these localities, veins and/or deformation bands were noted (Figure 12), which are absent from the other regional surface joints.

Table 2. Summary of straight scanline data for exposed fractures within the Mesaverde Group, Piceance basin, Colorado (empty cell indicates no data).

Scanline	Unit	Bedding Thickness	Mean Apparent Tracelength	Mean Penetration (Apparent) Depth	Linear Intensity
LB1	Lower WF	3.0 m (9.8 ft)		3.2 m (10.3 ft)	1.2 m^{-1} (0.4 ft^{-1})
LB2	Lower WF	2.4 m (8.0 ft)		~2.4 m (7.9 ft)	0.99 m^{-1} (0.3 ft^{-1})
LB3	Lower WF	1.1 m (3.4 ft)		~1.1 m (3.4 ft)	1.6 m^{-1} (0.5 ft^{-1})
LB5	Lower WF	4 m (13 ft)		3.2 m (10.3 ft)	0.65 m^{-1} (0.2 ft^{-1})
LB6	Lower WF	5.0 m (16 ft)		2.6 m (8.6 ft)	1.5 m^{-1} (0.5 ft^{-1})
WR3	Lower WF	1.0 m (3.2 ft)	>1.5 m (4.9 ft)	1 m (3.3 ft)	1.6 m^{-1} (0.5 ft^{-1})
WR4	Williams Fork	1.2 m (3.9 ft)		1.2 m (3.9 ft)	2.4 m^{-1} (0.7 ft^{-1})
ME1	Williams Fork	2.0 m (6.7 ft)	1.2 m (3.9 ft)	2 m (2.7 ft)	2.4 m^{-1} (0.7 ft^{-1})
CP East	Williams Fork			0.9 m (3.0 ft)	1.8 m^{-1} (0.5 ft^{-1})
CP West 1	Williams Fork				4.9 m^{-1} (0.5 ft^{-1})

Table 3. Circular scanline data for exposed fractures within the Mesaverde Group, Piceance basin, Colorado

Location	Mean Tracelength	Density	Intensity
Campbell pavement - Area 1	3.0 m (9.9 ft)	0.2 m^{-2} (0.01 ft^{-2})	0.5 m^{-1} (0.1 ft^{-1})
Campbell pavement - Area 2	2.3 m (7.4 ft)	0.1 m^{-2} (0.007 ft^{-2})	0.2 m^{-1} (0.1 ft^{-1})
Campbell pavement - Area 3	3.5 m (12 ft)	0.1 m^{-2} (0.01 ft^{-2})	0.5 m^{-1} (0.2 ft^{-1})
Meeker pavement	3.0 m (9.9 ft)	0.2 m^{-2} (0.02 ft^{-2})	0.6 m^{-1} (0.2 ft^{-1})
Wyatt pavement	1.6 m (5.2 ft)	4.6 m^{-2} (0.4 ft^{-2})	7.2 m^{-1} (2.2 ft^{-1})



Figure 12. High intensity fractures located near the Wyatt outcrop locality. The positive weathering/erosional relief is due to the presence of veins and/or deformation bands (arrows point to examples). This pattern and fracture frequency is unique to this locality and the CP West 1 locality and is believed to be fault related. GSA photo scale is 6.5 in (16.5 cm) long.

III. BOREHOLE-BASED ESTIMATORS FOR JOINT SIZE

Joints were sampled in the Mesaverde Group from 6 wells in the Piceance Creek gas field, near the axis of the Piceance Creek dome in the northern part of the Piceance basin (Figure 13). The company name, exact well locations and names, and exact depths of data are proprietary information. As the geometry and relative distribution of borehole joint traces as a function of lithology and formation are the key data, these proprietary aspects do not inhibit the analysis.

Formation MicroImager (FMI) Tool and Well-Logs

Joints were identified from images of borehole walls produced with the Schlumberger® Formation MicroImager (FMI) down-borehole tool (Figure 14), which is similar to Halliburton's Electrical MicroImaging (EMI) tool. As the FMI tool is pulled up the borehole, the upper electrode releases an electrical current that passes through the rock and is received by the lower eight pads (Figure 14). The recorded pattern of rock resistivity produces a borehole wall image that reveals lithology, bedding, cross beds, fractures, and even smaller features, such as laminations (Figure 15). This image is typically illustrated in a two-dimensional (2-D) form that is effectively an unwrapped cylinder (Figure 15). Therefore, a planar joint that intersects the borehole axis at a 90^0 angle produces a straight-line trace in the FMI log of the borehole wall (Figure 16a). If the joint is inclined at any other angle to the borehole axis, a sinusoid results, where the amplitude increases as the borehole angle to the joint decreases (Figure 16b).

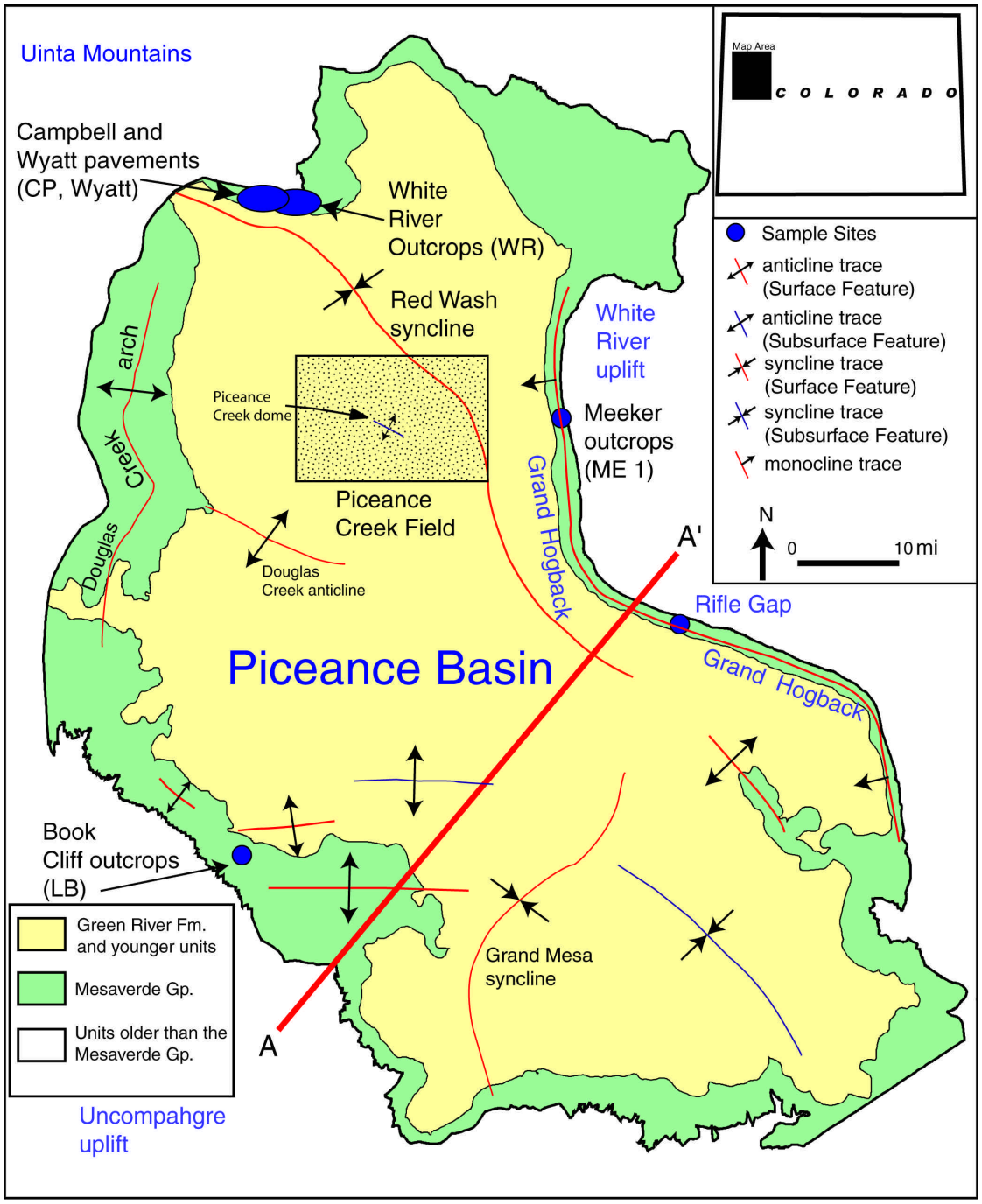


Figure 13. Location of the Piceance Creek gas field where the six sample wells are located (modified from Patterson et al., 2003).

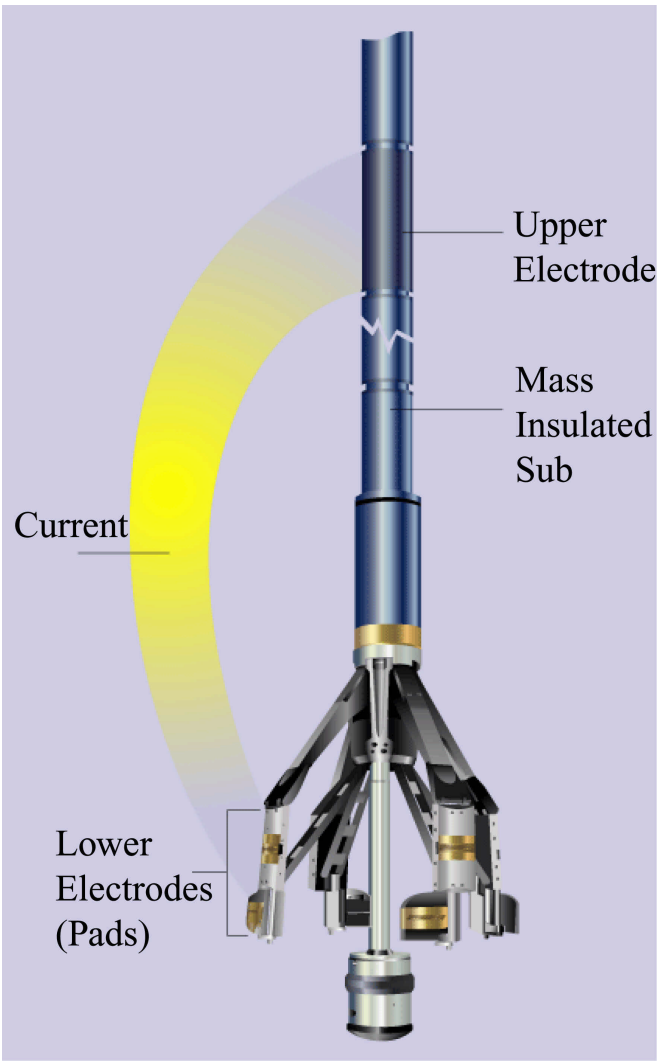
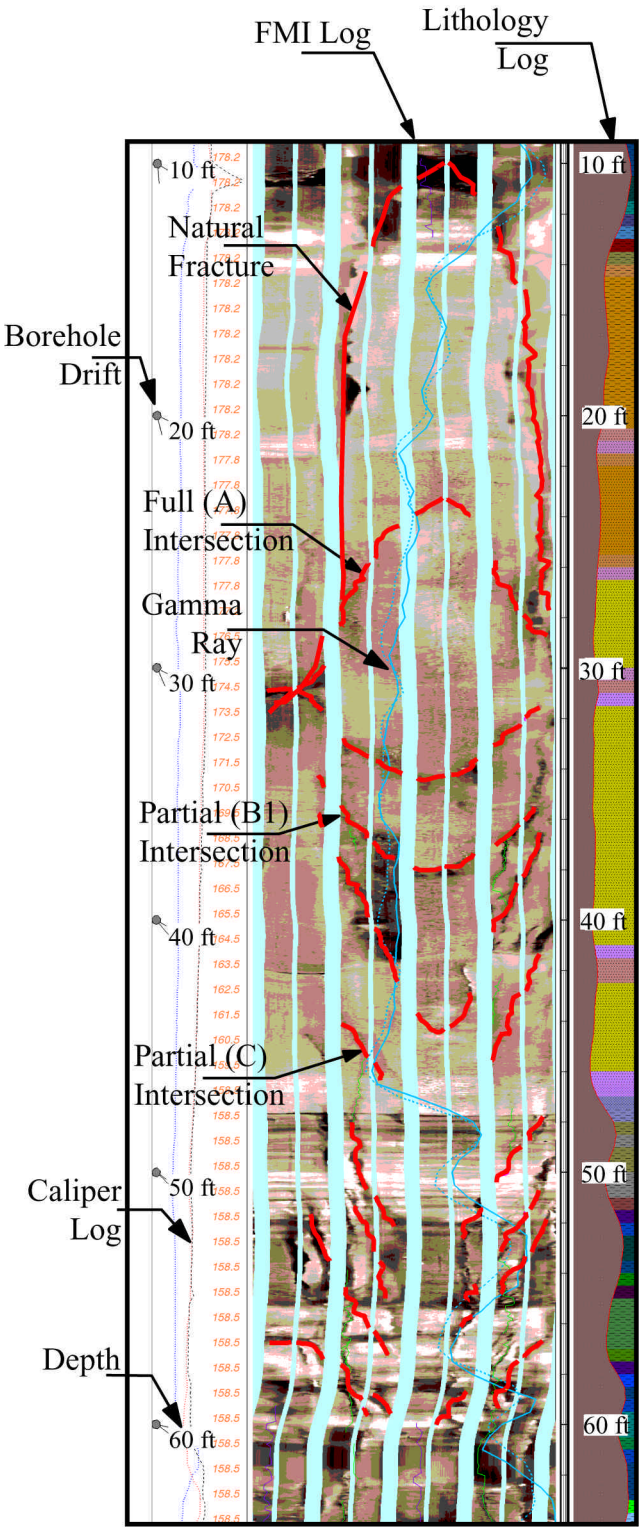


Figure 14. The Formation MicroImager tool. The FMI length in the figure is about 1.5m (5ft), and the entire length of the tool is ~7m (~24ft). (from Schlumberger website: www.slb.com).

Figure 15. Example FMI Log showing different fracture intersection types and other well log data. In the FMI image, the fractures are traced as they appear in the subsurface (red lines). Note the large size of the uppermost joint in the FMI log – joints of this size are not observed on the surface. The lithology log is determined by the volume of clay content and/or the gamma ray log (blue line). Additionally, the caliper log is shown, which is used to obtain the borehole diameter, and the borehole drift (not used in this study).


FMI Log
Lithology Log
10 ft
Natural Fracture
Borehole Drift
20 ft
Full (A) Intersection
Gamma Ray
30 ft
Partial (B1) Intersection
40 ft
Partial (C) Intersection
Caliper Log
50 ft
Depth
60 ft
10 ft
20 ft
30 ft
40 ft
50 ft
60 ft

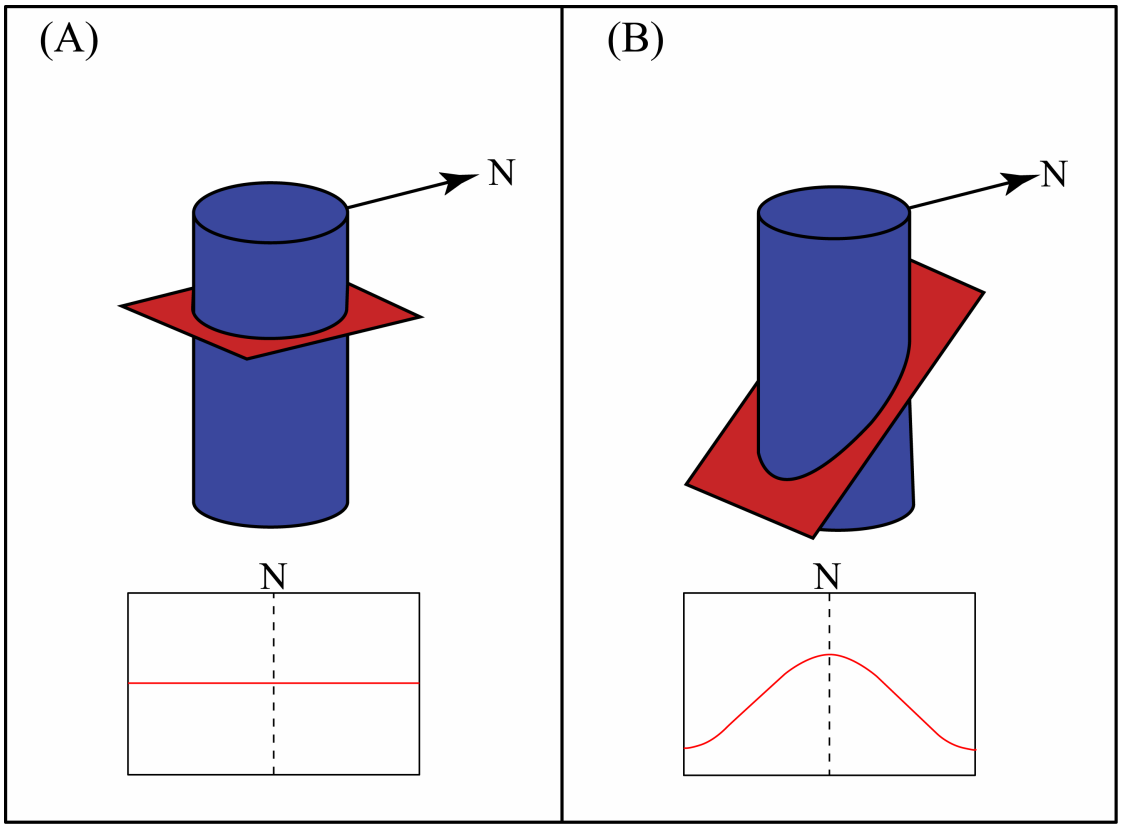


Figure 16. Examples of planar structure (i.e. fracture, bedding, etc.)/borehole intersections where (A) the plane is perpendicular to the borehole axis, and (B) inclined to the borehole axis.

Well logs contain other information, such as porosity data, other resistivity measures, caliper logs, and orientation data (Figure 15). This analysis only requires the traces of the joint intersections with the borehole, the borehole diameter obtained from the caliper logs, and the orientation data for the bedding and joints.

Joint Shape Assumption

The first step for estimating the joint size is to assume a geometric shape for the sampled fractures. Joints in nature are typically rectangular, circular, or elliptical, depending on the host lithology and thickness (Pollard and Aydin, 1988). Joint shape is site-specific and is a function of host lithologies and stress directions. Joints tend to terminate at discontinuities, such as bedding or older joints, unless enough stress existed to propagate across the discontinuity, or the discontinuity was sealed or closed (Pollard and Aydin, 1988). Lithologies with few planar discontinuities, such as massive sedimentary or crystalline rocks, tend to have joints that are either circular or elliptical (Pollard and Aydin, 1988). In thin- to medium-bedded sedimentary rocks, joints nearly normal to bedding commonly have two straight, bed-parallel edges where the joints terminate at the bedding surface (Gillespie et al., 2001; Rohrbaugh et al, 2002) and a straight, or slightly curved edges that connect these two, straight edges (Figure 17). Therefore, in bedded sedimentary rocks, joint shape is approximated as a square or a rectangle (Pollard and Aydin, 1988). Thus, as the joints in this study are contained within bedded sedimentary rocks, their shapes are assumed to be rectangular.

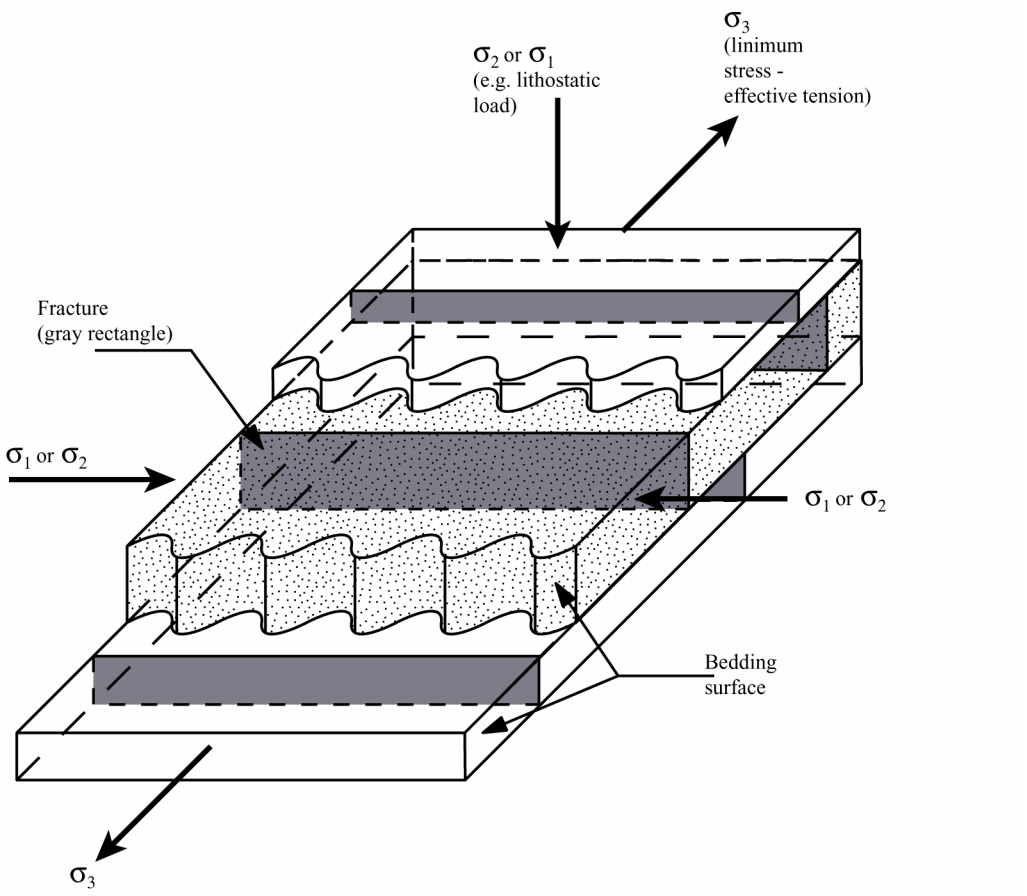


Figure 17. Block diagram showing typical bed-normal joint shapes in sedimentary rocks.

Borehole-Bedding-Joint Geometry

In the Piceance Creek gas field, the sampled boreholes are near vertical, the intersected bedding is near horizontal, and as with the surface joints, the master joints are approximately normal to bedding, and trend WNW. This geometric arrangement is presented in the following analysis, but is not required. Other geometric arrangements may be analyzed, typically with more complex trigonometric relationships as a function of more complex angular relationships between boreholes, bedding and joints, but the approach that we present would still be applicable. Also, for the case of the Piceance Creek gas field, the joint bedding intersections (bed-parallel intersections) may be the long (L) or short (W) edges of the rectangle. While intuitively, the long edge might be expected to be the bed-parallel intersect (Figure 17), this geometry is not necessitated in nature or in this analysis.

Joint/Borehole Intersection Geometries

The subsurface joints are sampled along boreholes that have an average diameter of about 0.3 m (11.8 inches), which is typically much smaller than the average joint size. The fact that only a small fraction of each joint is sampled has limited previous attempts at determining joint size from borehole data. The present analysis utilizes a new approach based on the recognition of different intersection types: complete, edge, or piercing (Figure 18).

The observed joint intersection types on the borehole wall are a function of joint geometry, orientation, shape, and position with respect to the borehole (Figures

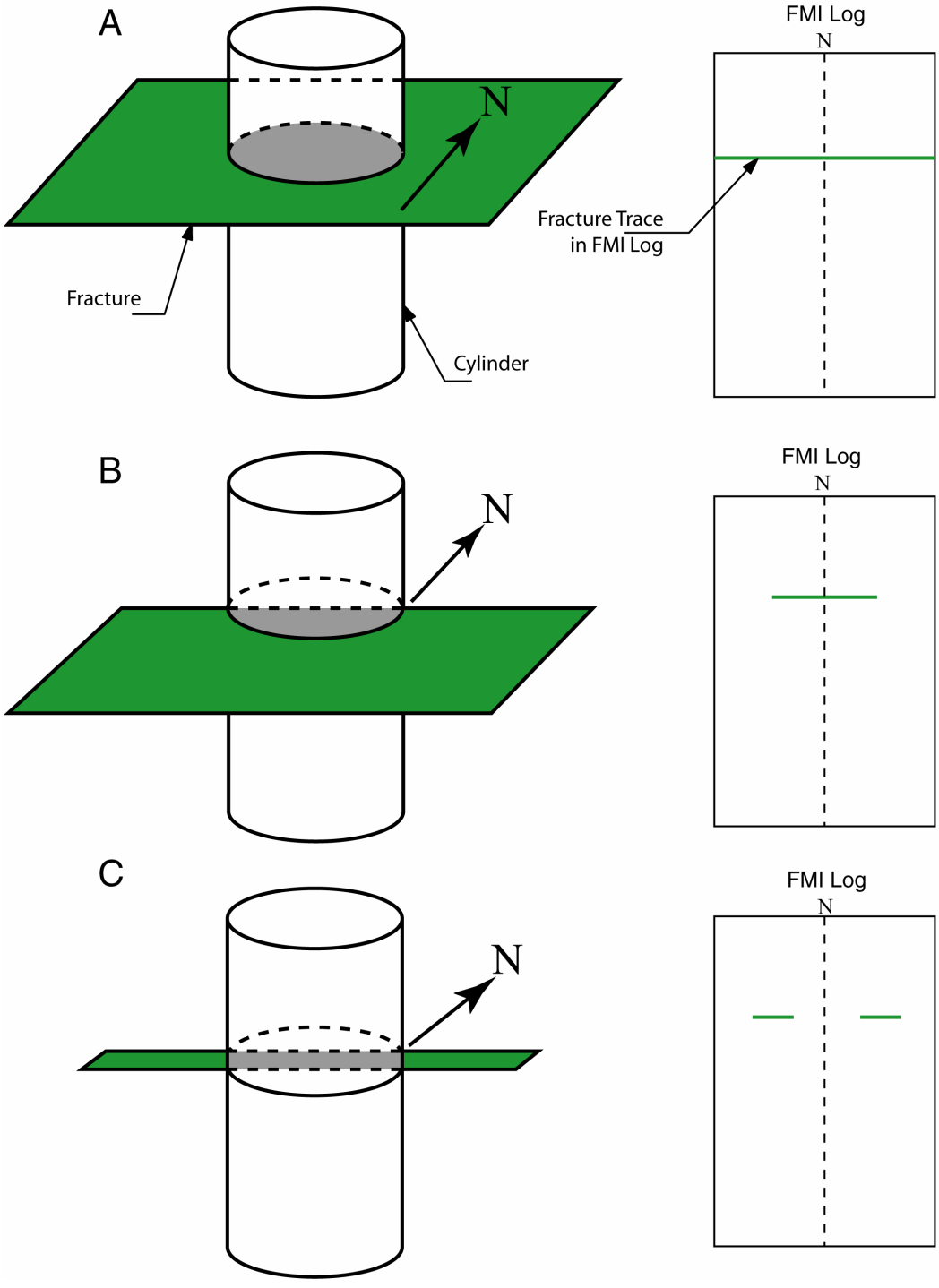


Figure 18. Complete (A), edge (B), and piercing (C) joint/borehole intersections for the case of joints normal to the borehole axis.

15, 16, 18, 19). For the analysis, the joints could be treated separately, but treating them collectively by projecting them into a common plane normal to the borehole axis is more useful (Figure 20). The main advantage of this approach is that the intersection types may be considered collectively in terms of the loci of the centers of possible boreholes that could intersect the joint (Figures 19, 21, 22). The presence and shape of the intersection loci is a function of whether the projected width, W', is greater than or less than the borehole diameter, D (Figures 20, 21, 22).

The relative abundances of the intersection types on borehole walls is a function of the relative sizes of the areas for the intersection loci (Figures 21, 22). As the size of these intersection loci depends on borehole diameter and fracture size, the relative sizes of these loci and hence, the independent intersection counts can be used to estimate joint size. Using the relative abundances of the complete, edge, and piercing intersection types to estimate joint size is a key conceptual advance from this analysis.

Complete (A) Intersections

An A-intersection is where a borehole completely transects the joint (Figures 18a and 19) and is characterized by a complete joint trace in the FMI log (Figures 15, 18a, and 19, Table 4). Thus, this intersection type requires that the projected width, W', is greater than the borehole diameter, where

$$W' = W \cos\theta, \tag{1}$$

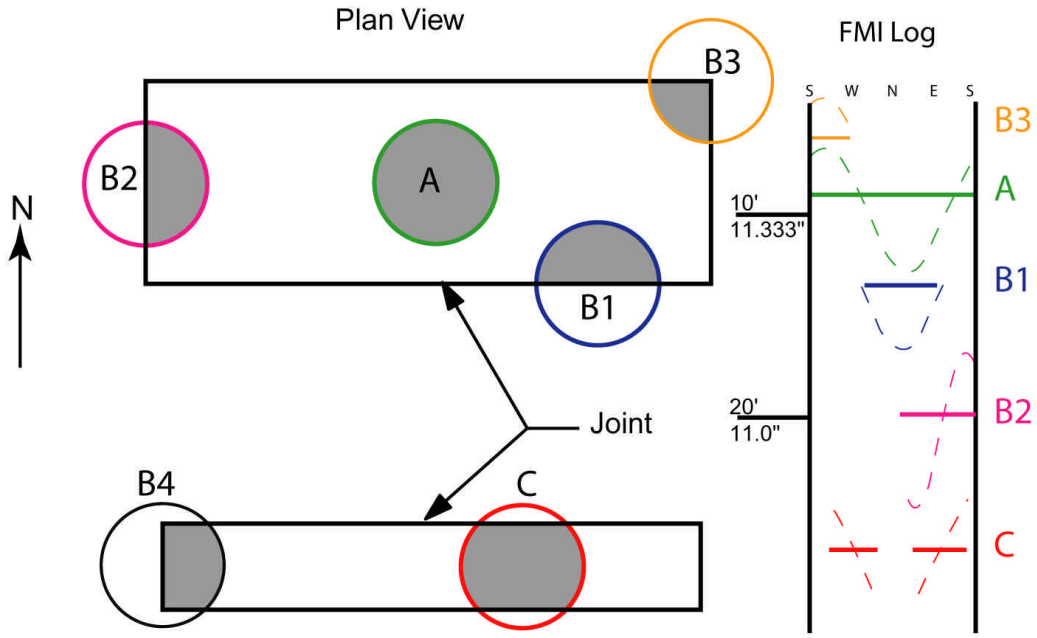


Figure 19. Plan view of borehole intersection types for a borehole-normal joint. For this example, L is trending E-W for a joint (solid rectangle) of W'>D (top) and W'<D (bottom). On the right is the intersection trace on an FMI log with geographic coordinate. Each intersection is identified on the joint and in the FMI Log. The solid lines are the traces for borehole-normal joints, whereas the dashed lines are joint traces for joints inclined to the borehole axis at greater than 0º and less than 90º.

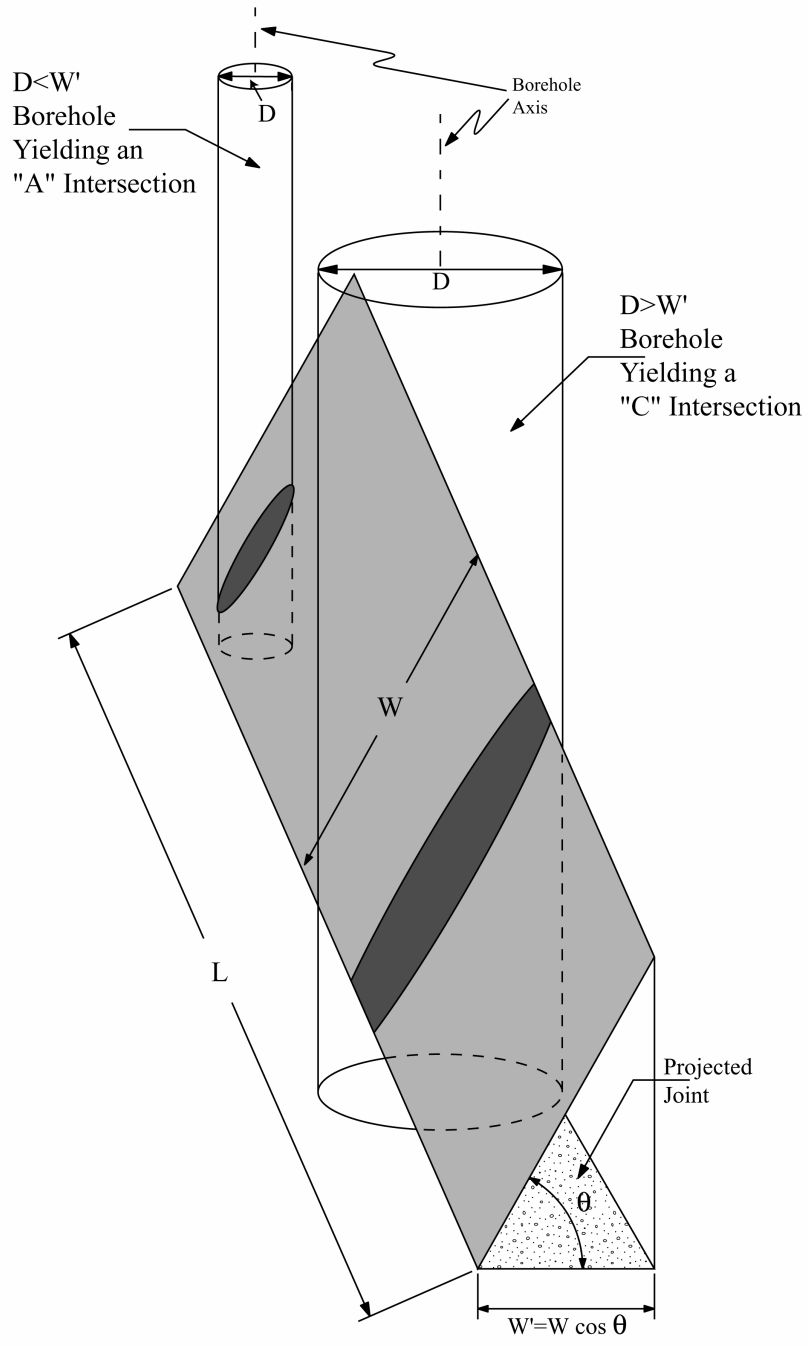


Figure 20. Geometry of a joint inclined to the borehole axis and the corresponding projected joint. Here, the long edge of a joint, L, contained in bedding is normal to the axis of an intersecting borehole, such that when the joint is projected into a plane normal to the borehole axis, the new plane has width, W'. If W rather than L was normal to the borehole axis, then W'=L cos θ.

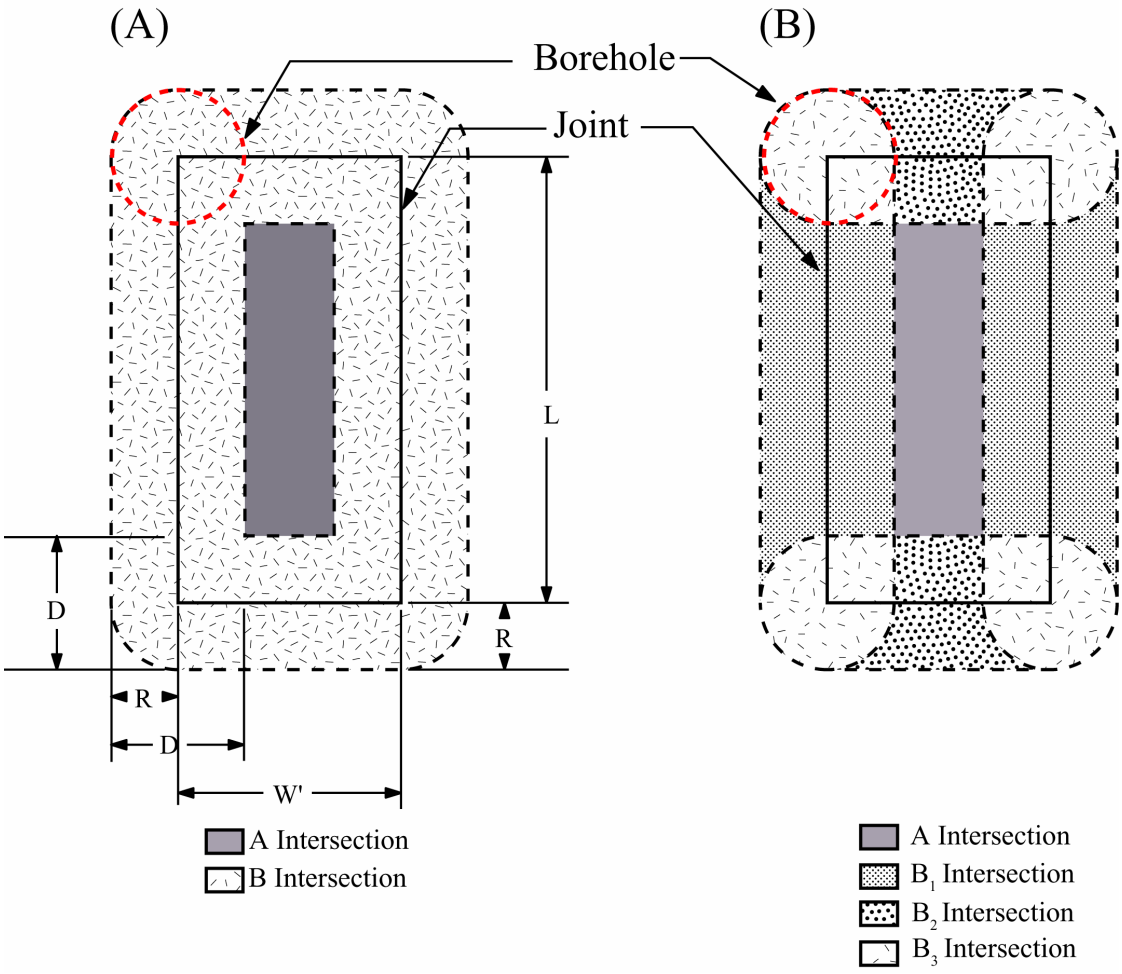


Figure 21. Loci of centers of boreholes with different intersection types on a rectangular joint (heavy solid line) projected onto a plane normal to the borehole axis where D<W. (A) A and B loci; and (B) A, B_1, B_2, and B_3 loci. D is the borehole diameter, R is the radius, W' is the projected joint width, and L is the length.

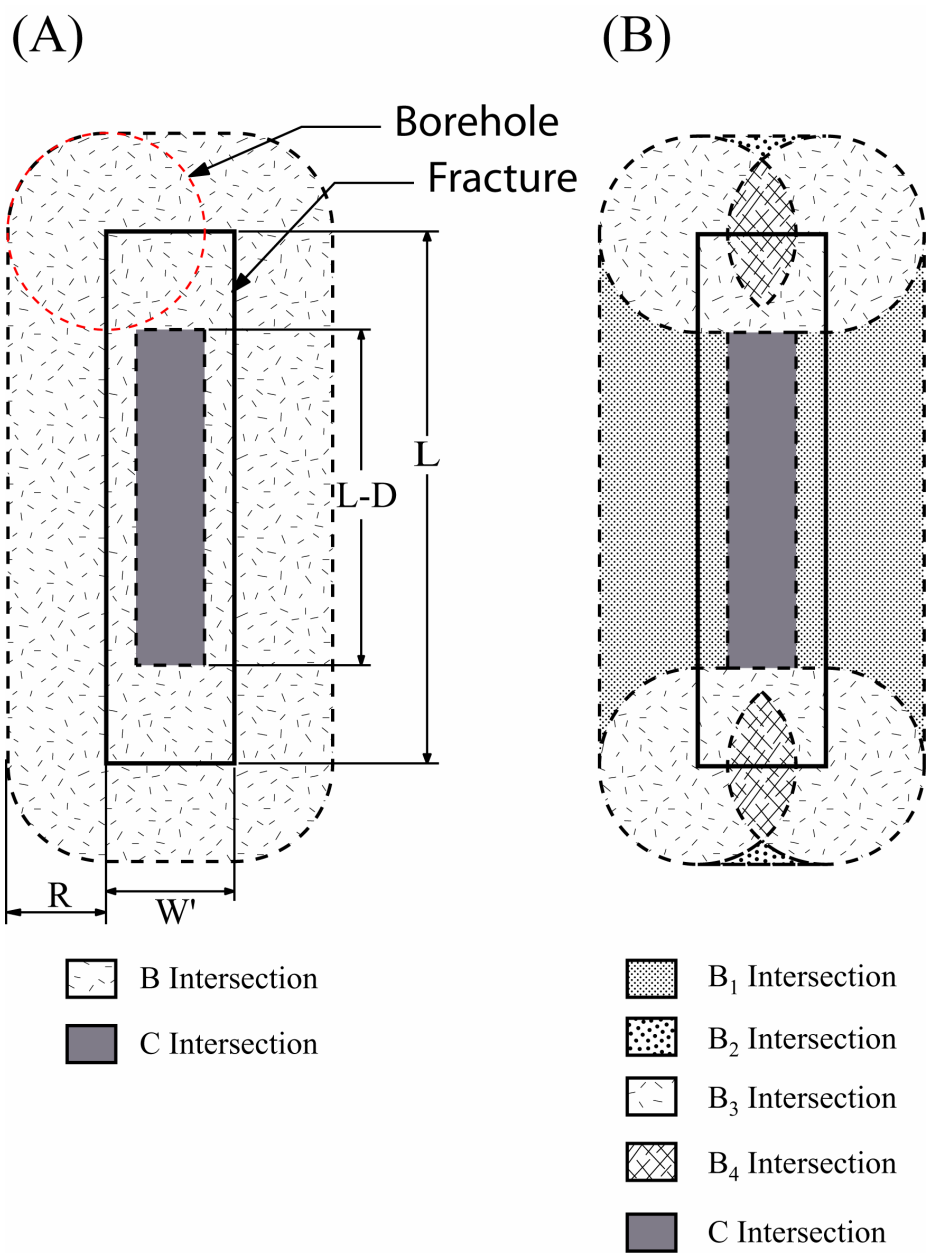


Figure 22. Loci of centers of boreholes with different intersection types on a rectangular joint (heavy solid line) projected onto a plane normal to the borehole axis where D>W (borehole example is red dashed circle). (A) B and C loci; (B) B_1, B_2, B_3, B_4, and C loci, D is the borehole diameter, R is the radius, W' is the projected joint width, and L is the length

Table 4. Joint/Borehole intersection definitions and characteristics

Intersection Type	**Definition**	**FMI Characteristics for a vertical borehole**
A (green-colored circle and trace in Figure 19)	Borehole completely intersects joint	Complete trace
B (Blue, Pink, and Yellow)	Borehole partially intersects joint	One trace segment not completely extending across log
B_1 (Blue)	Borehole intersects bed-parallel edge (L)	One trace segment centered about dip direction or 180^0 from dip direction
B_2 (Pink)	Borehole intersects joint edge that penetrates bed, or dipping edge (W)	One trace segment centered about fracture strike
B_3 (Yellow)	Borehole intersects joint corner intersects	One trace segment not symmetric or centering about dip or strike
B_4	W' < D and Borehole intersects joint end	Identical to B_2 intersection in log
C (Red)	W' < D and fracture pierces borehole	Two opposite traces in log

with *W* the joint width and θ is the angle difference between the joint normal and the borehole axis. For the case of a vertical borehole, θ is the dip.

A-intersections, like all joint intersections, are a function of the borehole diameter and the fracture size. For a projection of a rectangular joint (LxW') into the plane normal to the borehole axis, an inner area exists within the joint where the center of a borehole of diameter, D, falls so as to obtain an A intersection (Figure 21a). The area is

$$Area_A = (W'-D)(L-D)\,. \tag{2}$$

Pierced (C) Intersections

Pierced intersections, labeled C-intersections, occur where a projected rectangular joint (LxW') has a projected width (W') less than the borehole diameter, so that the borehole intercepts both long edges of the joint plane (Figures 18c, 19, and 20). In the FMI log, a C-intersection is characterized by two fracture traces on the borehole wall (Figures 15, 18c, 19, 20, Table 4). For a joint projected into the plane perpendicular to the borehole axis, the inner intersection area of the joint where a borehole center is located to obtain a C-intersection is (Figure 22):

$$Area_C = (D-W')(L-D)\,. \tag{3}$$

Edge (B) Intersections

Edge and corner intersections are referred to as B intersections (Figures 18b and 19) that are characterized by single partial traces in the FMI log (Figures 15, 16b, and 19). The areas for the loci of all B intersections are functions of the relative sizes of W' and D (Figures 21a, 22a). So, when W'>D

$$Area_B = 2(L + W')D - D^2 + D^2 \frac{\pi}{4}\ , \tag{4}$$

and when W<D

$$Area_B = 2LW' + \left(1 + \frac{\pi}{4}\right)D^2 . \tag{5}$$

B_1 Intersections. Edge intersections along the joint length are B_1 intersections (Figure 19, Table 4). The two intersection areas (Figures 21b, 22b) are:

$$Area_{B1} = 2(L - D)D + D^2 - D^2 \frac{\pi}{4},\ \text{for W'>D} \tag{6}$$

$$Area_{B1} = (DL - D^2 \frac{\pi}{4}) + (L - D)(2W - D),\ \text{for W'<D.} \tag{7}$$

In the FMI logs, B_1 intersections appear as joint traces that are symmetric about the dip direction or 180º from the dip direction (Figure 19, Table 4). For

example, if a fracture dips north and the borehole intersects the northern bed-parallel edge, the resulting trace will be a line segment symmetric about the north, or south direction in the FMI log (blue circle and trace in Figure 18 symmetric about the north-direction).

B_2 Intersections. B_2 intersections are borehole/joint intersections along the true width, W, or for a projected joint along W' (Figure 19, Table 4). The intersection areas (Figures 21b, 22b) are:

$$\text{Area}_{B2} = 2(W'-D)D + D^2 - \pi\frac{D^2}{4}, \text{ for } W'>D \tag{8}$$

$$Area_{B2} = W'D - \pi\frac{D^2}{4} + D^2\cos^{-1}\left(\frac{W'}{D}\right) - W'\sqrt{D^2-(W')^2}, \text{ for } W'<D \tag{9}$$

B_2 intersections occur as joint traces that center between the dip direction and its opposite, and may have a form that may include both apexes of the partial sinusoid. (Figure 19, Table 4). For example, a fracture that strikes E-W intersected by a borehole along the westernmost side of the fracture (see pink borehole in Figure 19) yields a single trace in the FMI log that centers about the west direction (pink trace, Figure 19).

B_3 Intersections. Corner intersections are B_3 intersections (Figure 19, Table 4). The intersection areas are (Figures 21b, 22b):

$$Area_{B3} = 3\pi\frac{D^2}{4} + D^2, \quad \text{for W'>D} \tag{10}$$

$$Area_{B3} = \pi\frac{D^2}{2} + 2W'D - \left(Area_{B2} + Area_{B4}\right), \quad \text{for W'<D.} \tag{11}$$

B_3 borehole/joint intersections are partial traces that do not center with respect to joint orientation (yellow trace Figure 19; Table 4).

B_4 Intersections. Joint end intersections are B_4 intersections (Figure 19, Table 4) and occur when the projected width, W', is less than the borehole diameter. The intersection area (Figures 22b) is:

$$Area_{B4} = D^2 \cos^{-1}\left(\frac{W'}{D}\right) - W'\sqrt{D^2 - W'^2} \tag{12}$$

The appearance of this intersection type in the FMI log is essentially identical to a B_2 intersection in that the borehole intersects the projected joint width, which yields a partial line segment that centers about the fracture strike direction (Figure 19, Table 4). For this reason, B_4 intersections are indistinguishable from B_2 intersections, and thus, are not separately identified during a count of intersection types in a well.

Joint Size Estimators

Consider first the case of a set of identical, parallel, rectangular joints arranged according to any configuration in a rock mass (Figure 23). Next assume that the rock mass sample space is penetrated by one or more boreholes located independently of the array of fractures (Figure 23). Each joint has a projected joint of dimensions LxW' (Figure 20) that is perpendicular to the borehole axis (Figure 24). Each of these projected fractures have intersection areas that are a function of the borehole size and fracture size (Figures 21, 22, 25). The B intersection (edge) areas – to take a specific example – are considered in aggregate as the "projected B region" (Figure 25). Each occurrence of the borehole axis penetrating the B intersection area constitutes a B – intersection. Because the B intersection area is determined by the borehole size and the fracture size, the expected number of B intersections, for the estimators were developed for three cases:

Case 1: W'>D where L and W are constant,

Case 2: W'<D where L and W are constant, and

Case 3: L and W are not constant, so W' varies with respect to D.

Case 1

Only A, B_1, B_2, and B_3 intersections occur for Case 1 (Figures 15, 18, 19, 20, 21). Given two unknowns, L and W, a system of two simultaneous equations is required to achieve a solution and two ratios of areas may be used to establish a system of solvable simultaneous equations. Considering the case of $Area_B$ to $Area_A$:

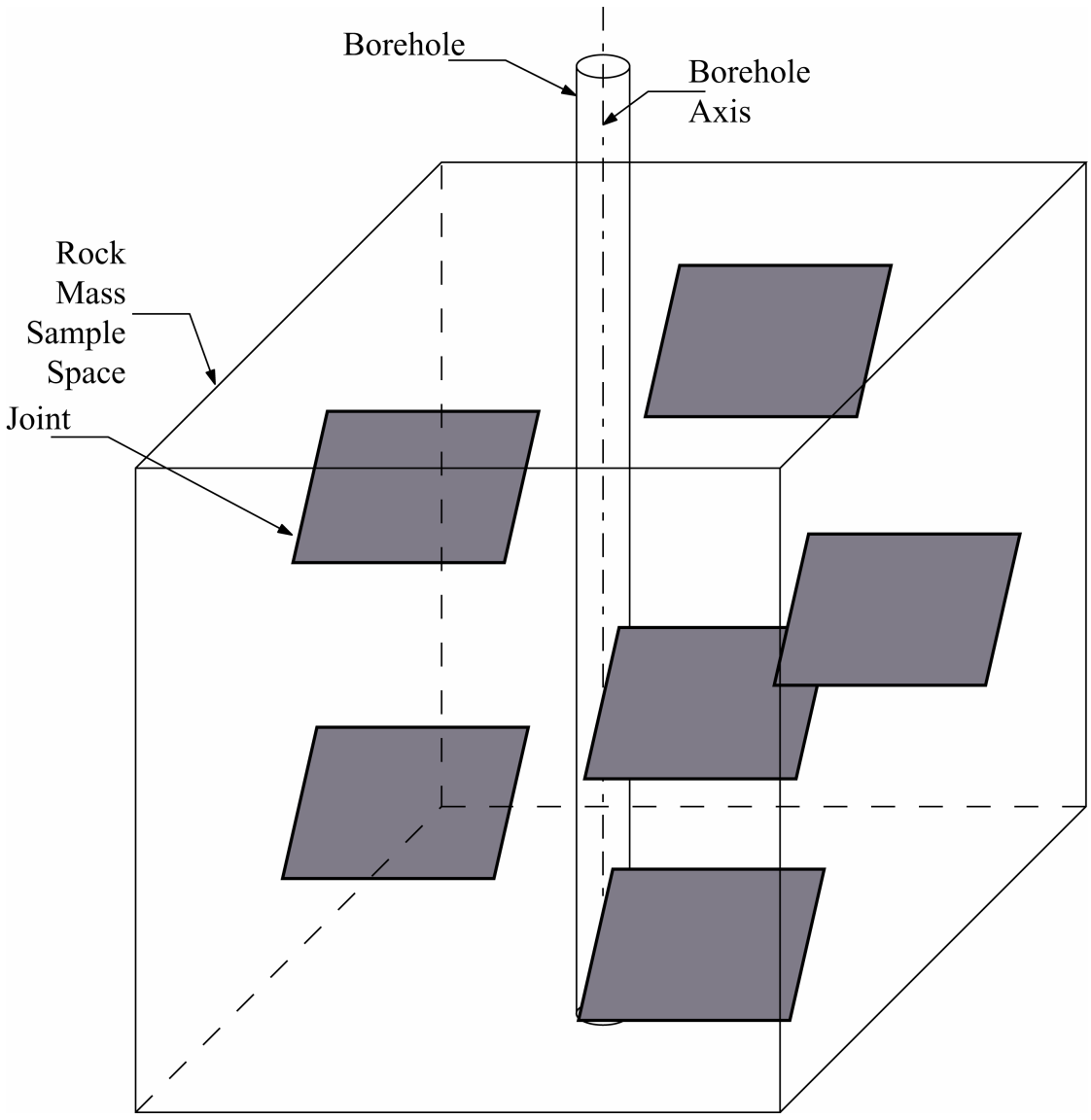


Figure 23. Rock mass (cube) containing identical, parallel, rectangular joints penetrated by a borehole of diameter D.

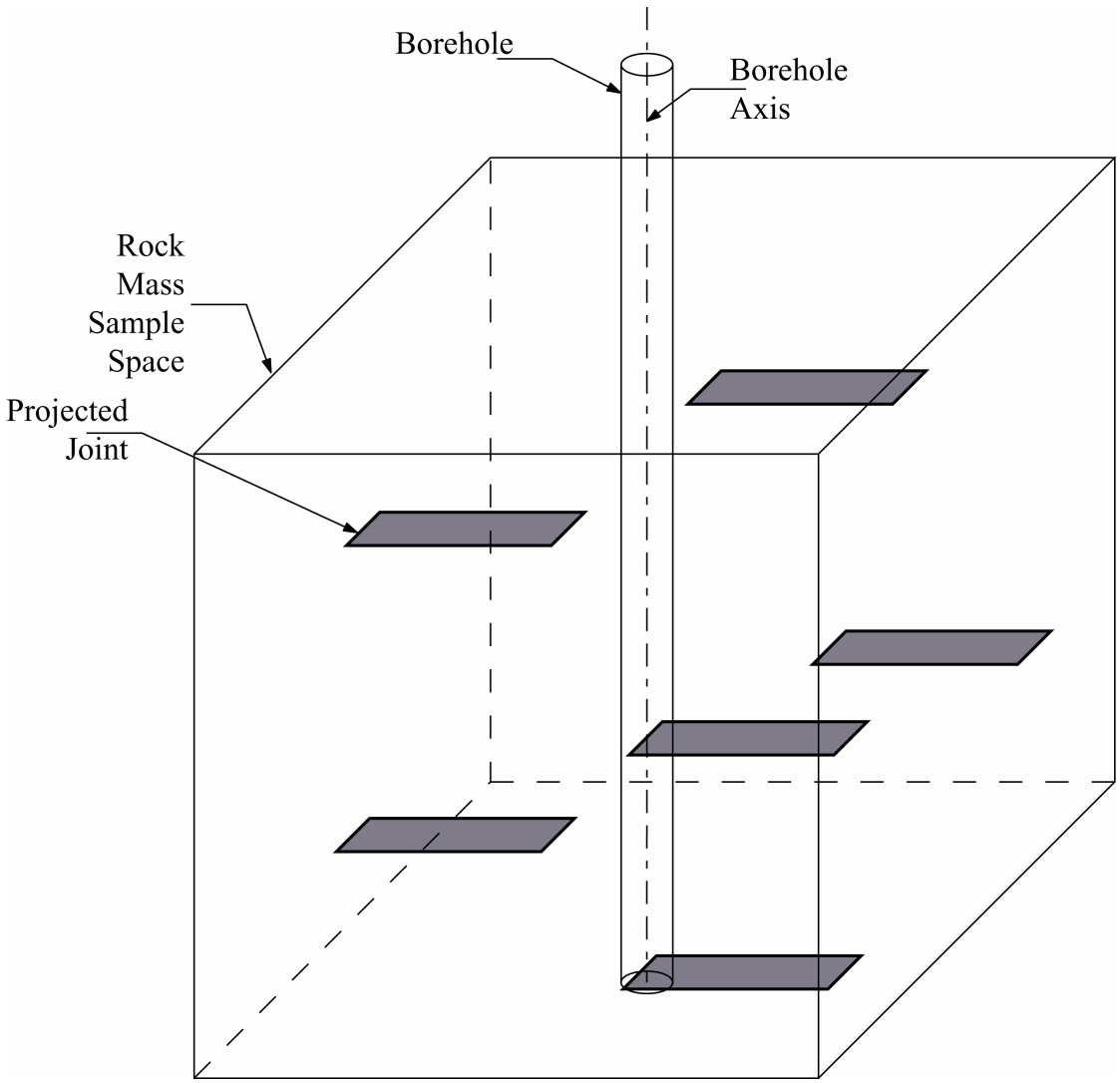


Figure 24. Projected joints within rock mass of Figure 23.

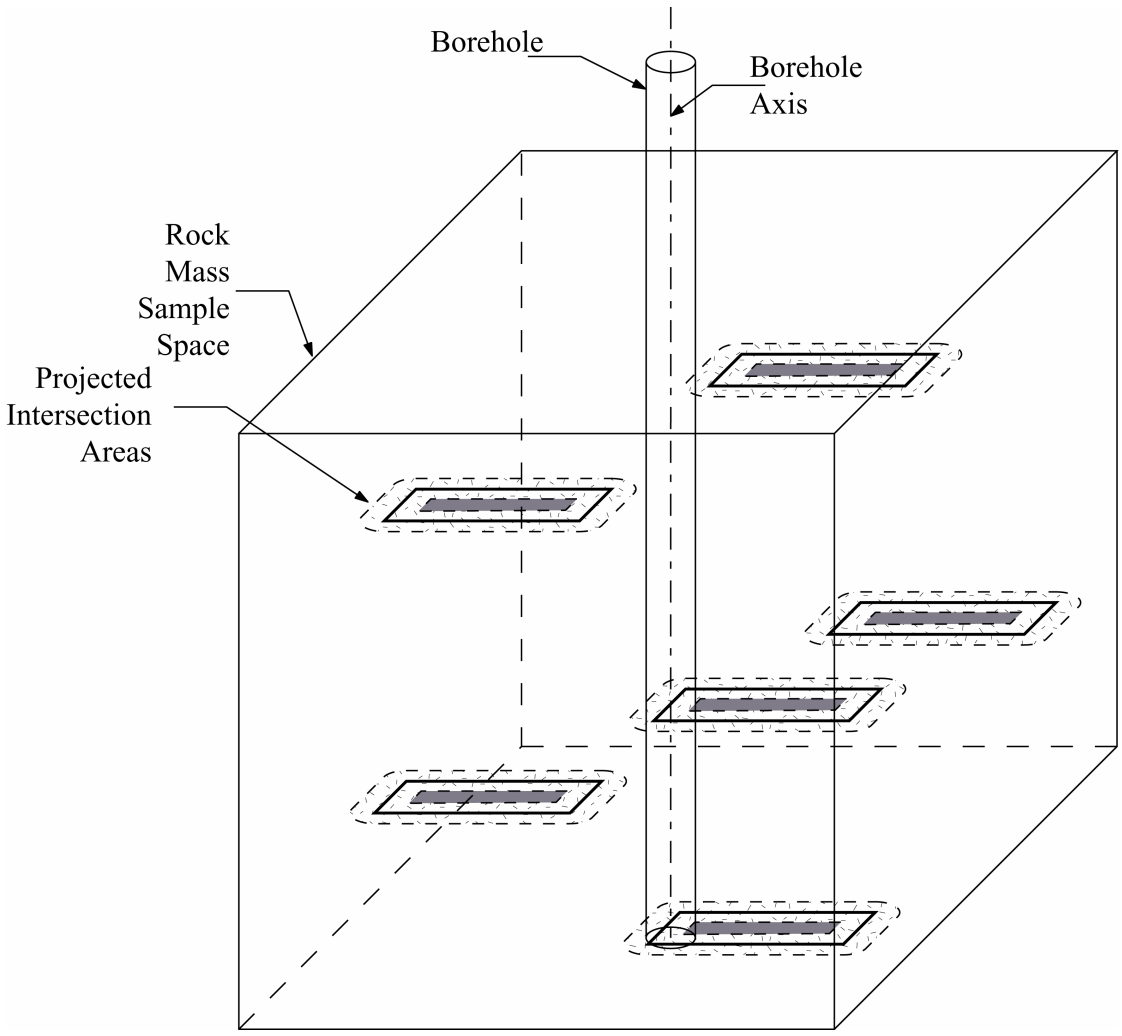


Figure 25. Corresponding intersection areas for the projected joints in Figure 24. The projected fractures of Figure 24 have associated intersection areas or “projected intersection areas” which are a function of the borehole diameter and fracture size.

$$\frac{\widetilde{N}_B}{\widetilde{N}_A} = \frac{Area_B}{Area_A} = \frac{2(\mathrm{L} + \mathrm{W}')\mathrm{D} - \mathrm{D}^2 + \pi\frac{\mathrm{D}^2}{4}}{(\mathrm{W}'-\mathrm{D})(\mathrm{L} - \mathrm{D})} \quad , \tag{13}$$

where $\widetilde{N}_A$ is the number of B intersections, $\widetilde{N}_A$ is the number of A intersections, and the numerator is Equation 4 and the denominator is equation 2. Considering a second ratio for Area_{B1} (Equation 6) relative to Area_{B2} (Equation 8):

$$\frac{\widetilde{N}_{B1}}{\widetilde{N}_{B2}} = \frac{Area_{B1}}{Area_{B2}} = \frac{2(\mathrm{L} - \mathrm{D})\mathrm{D} + \mathrm{D}^2 - \pi\frac{\mathrm{D}^2}{4}}{2(\mathrm{W}'-\mathrm{D})\mathrm{D} + \mathrm{D}^2 - \pi\frac{\mathrm{D}^2}{4}}, \tag{14}$$

where $\widetilde{N}_{B1}$ is the number of B_1 intersection counts, and $\widetilde{N}_{B2}$ is the number of B_2 intersection counts. The "knowns" are the intersection counts, which are measured, and the diameter, which is provided by the caliper log (Figure 15). Rewriting Equation 14 in terms of L:

$$L = \left(\frac{\widetilde{N}_{B1}}{\widetilde{N}_{B2}}\right)W' - \frac{\left(1+\frac{p}{4}\right)D}{2}\left(\frac{\widetilde{N}_{B1}}{\widetilde{N}_{B2}} - 1\right), \tag{15}$$

and substituting Equation 15 into Equation 13 yields a quadratic equation in the form of $a_{w'}x^2+b_{w'}x+c_{w'}=0$, where x=W', and the coefficients $a_{w'}$, $b_{w'}$, and $c_{w'}$ are (see appendix A for derivation):

$$a_{w'} = \left(\frac{\widetilde{N}_{B1}}{\widetilde{N}_{B2}}\right)\left(\frac{\widetilde{N}_{A}}{\widetilde{N}_{B}}\right) \tag{16a}$$

$$b_{w'} = -D\left[\frac{\widetilde{N}_{A}}{\widetilde{N}_{B}}\left(\frac{1+\frac{\pi}{4}}{2}\left(\frac{\widetilde{N}_{B1}}{\widetilde{N}_{B2}}-1\right)+1+\frac{\widetilde{N}_{A}}{\widetilde{N}_{B}}\right)+2\left(\frac{\widetilde{N}_{B1}}{\widetilde{N}_{B2}}+1\right)\right] \tag{16b}$$

$$c_{w'} = D^2\left[\frac{\widetilde{N}_{A}}{\widetilde{N}_{B}}\left(\frac{1+\frac{\pi}{4}}{2}\left(\frac{\widetilde{N}_{B1}}{\widetilde{N}_{B2}}-1\right)+1\right)+\left(1+\frac{\pi}{4}\right)\left(\frac{\widetilde{N}_{B1}}{\widetilde{N}_{B2}}-1\right)+1-\frac{\pi}{4}\right]. \tag{16c}$$

So,

$$W' = \frac{-b_{w'} \pm \sqrt{b_{w'}^{\,2} - 4(a_{w'})(c_{w'})}}{2a_{w'}}. \tag{17}$$

Typically, only one real root exists and that is the value for mean W'. Mean L is estimated by substituting W' into Equation 15, and true W is calculated from the value for W' using Equation 1.

Case 2

The Case 2 scenario involves fractures that have W'<D (Figures 18c, 19, 22) and thus, only B_1, B_2, B_3, B_4 and C intersections are possible. Using the same logic as in Case 1, the relative abundance of the B to C intersection counts, $\frac{\tilde{N}_C}{\tilde{N}_B}$, is related to the fracture L and W', by comparing their respective areas (dividing Equations 3 by 5):

$$\frac{\tilde{N}_C}{\tilde{N}_B} = \frac{(D-W')(L-W')}{2LW'+\left(1+\frac{\pi}{4}\right)D^2}. \tag{18}$$

C-intersections are defined as fractures that pierce the borehole, and thus have their entire width contained in that borehole (Figures 18c, 19, 20, 26), which is determined using simple trigonometric calculations. For this intersection type, two traces are revealed in the FMI log and each trace has endpoints referred to as p_1 and p_2 (Figure 26). For geometric purposes, a y-axis is established, which is parallel to the fracture dip direction and is closest to the p_1 endpoint (Figure 26). The y-axis is θ_1 and θ_2 degrees away from p_1 and p_2, respectively (Figure 26). Determining the projected joint width, W', from this geometry:

$$W' = \left|\cos\theta_1 - \cos\theta_2\right|\frac{D}{2}. \tag{19}$$

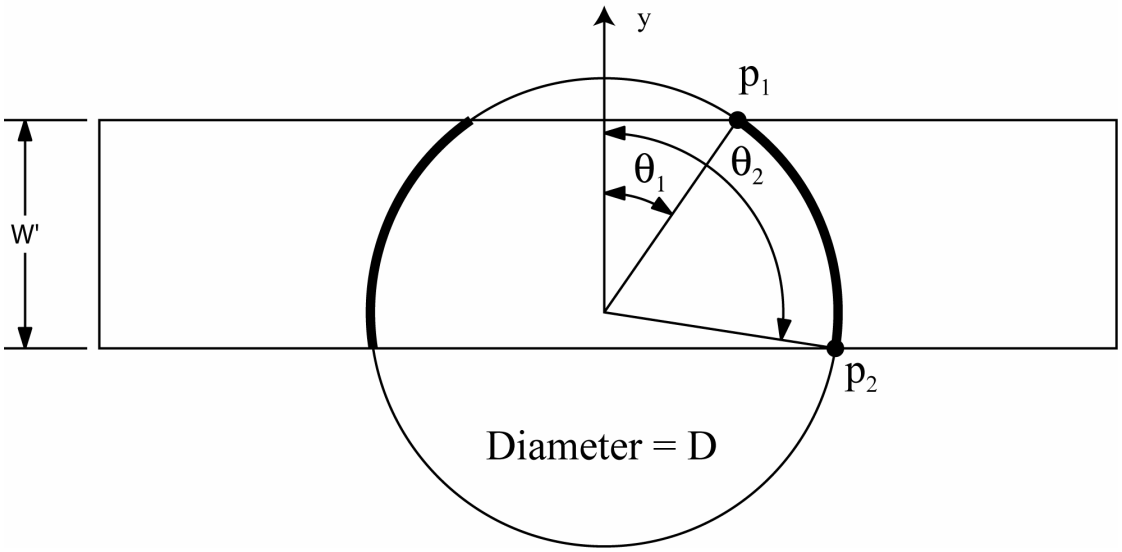


Figure 26. Width determination from a C intersection. The bold lines represent the two traces in the FMI log from the borehole wall, p_1 and p_2 are the locations of the end points of the traces in the FMI log, and θ_1 and θ_2 are the angles between these points and the y-axis, which is parallel to the fracture width. (modified from Wang et al., 2004)

Widths for individual fractures are obtained for each C-interesection in the log. The projected width is then determined for the joint set (Equation 19) and substituted into Equation 18 to yield *L*. True *W* is then calculated from the value for *W'* using Equation 1.

Case 3

For this case, where *W* and *L* are not constant, a population of joints have values for *W'* that span the range from less than to greater than *D* (Mauldon and Wang, in prep; Appendix B). The derivation for the estimators for this case yields a system of three equations (Appendix B, Equations B-5, B-6, B-7) with five variables λ, a, $\mu_{W'}$, μ_L, and $E[l^2]$, where λ is an intensity measure, a is the aspect ratio, $\mu_{W'}$ is the mean projected width, μ_L is the mean length, and $E[l^2]$ is the second moment of the probability distribution of l. a is defined as the aspect ratio (L/W) or

$$\alpha = \frac{\mu_L}{\mu_{W'}} \tag{20}$$

For a population of fractures, it is reasonable to assume that the fractures of a given set generally keep the same shape, meaning that there is a relationship between joint length and width, and thus the aspect ratio will not vary much. Thus, a is assumed to be constant and as a is a function of μ_L and $m_{W'}$, only four variables are left.

λ is an intensity measure defined as the number of fractures per unit area. If there is no preference as to the number of any sized fracture, then we can assume the same number of fractures for each size and λ would be constant. From stereology (Appendix B), λ is shown to be

$$\lambda = \frac{H \cdot P_{32}}{\mu_L \mu_{W'}} \tag{21}$$

where H is the borehole length, P_{32} is the volumetric intensity, and thus is defined in terms of μ_L and $\mu_{W'}$. Cycloidal scanlines are utilized to estimate P_{32} from borehole data (Mauldon and Wang, 2003) and the estimator is presented in Appendix C. The variable $E[l^2]$ is included in the Equations B-5 and B-23 (Appendix B). When Equation B-5 is subtracted from Equation B-23, the term disappears. Therefore, the system of equations now has 2 unknowns, μ_L and $\mu_{W'}$, and may be solved simultaneously.

Solving the system yields a quadratic equation in $\mu_{W'}$ (Appendix B) with coefficients

$$a_{W'} = \widetilde{N}_{B1} + 2\widetilde{N}_C, \tag{22a}$$

$$b_{W'} = \pi\left(\widetilde{N}_{B1} + 2\widetilde{N}_C\right)\frac{D}{4} + \left(\widetilde{N}_B - \widetilde{N}_{B1}\right)(4+\pi)\frac{D}{8} - 2HP_{32}D, \tag{22b}$$

$$c_{W'} = \frac{-\pi H P_{32} D^2}{2}, \tag{22c}$$

Solving for $\mu_{W'}$ (Appendix B)

$$\mu_{W'} = \frac{-b_{W'} + \sqrt{b_{W'} - 4a_{W'}c_{W'}}}{2a_{W'}}, \text{ and} \tag{27a}$$

yields a value for $\mu_{W'}$ that may be substituted into

$$\mu_L = \frac{\widetilde{N}_{B1} + 2\widetilde{N}_C}{\widetilde{N}_B - \widetilde{N}_{B1}}\left(\mu_{W'} + \frac{\pi D}{4}\right) + (4+\pi)\frac{D}{8}, \tag{27b}$$

to determine *L*, and *W* is determined using Equation 1.

IV. SIMULATION RESULTS

The Case 1 and Case 2 size estimators were applied to simulated joints where all input values were known and could be controlled, using a visual C++ programming environment to conduct a Monte Carlo analysis (Wang et al., 2004). The simulation generates parallel rectangular joints in either a cubical, spherical, or cylindrical generation volume (Figure 27).

For a simulation run, joint length and width, borehole diameter and length, sampling volume, joint orientation, and joint intensity are specified. The intersection counts produced in each run were summed through a series of runs for the same parameter set, so as to yield a cumulative intersection count total. The summing approach allows investigation of estimator performance as a function of the number of counts.

Case 1

Three simulations of 300 runs were performed (Figure 28, Table 5). Joints where assumed to be normal to the borehole axis, so that W'=W (Equation 1), and Equations 13 and 14 were used to estimate L and W. For a single run, the average number of intersections counts are $\widetilde{N}_A$: 51, $\widetilde{N}_B$: 61, $\widetilde{N}_{B1}$: 51, $\widetilde{N}_{B2}$: 6, and $\widetilde{N}_{B3}$: 5, which typically yield estimates with an average variance of 10.6 and 0.2 from the expected lengths and widths, respectively. As the runs accumulated for each simulation, the estimates tended to within 2% of the expected values (Figure 28, Table 5), demonstrating that the Case 1 estimators can accurately predict L and W.

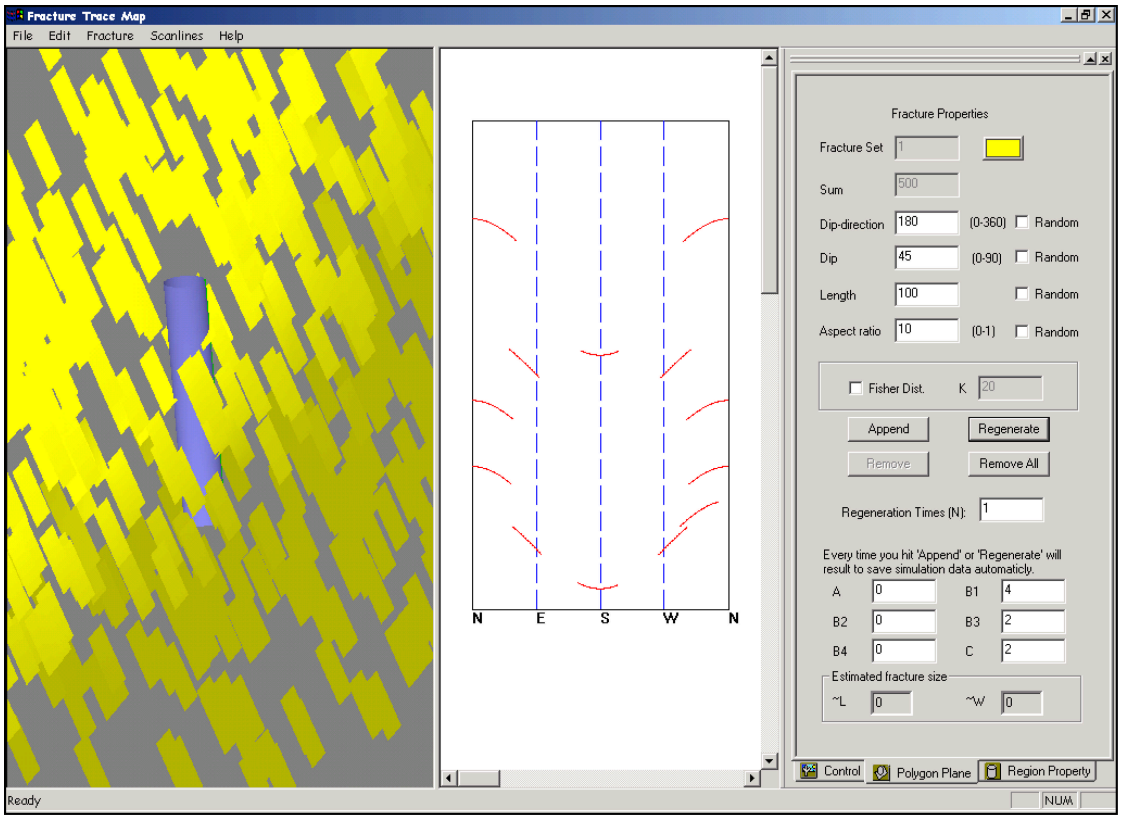


Figure 27. Graphical interface for the joint simulation program. The program applies user-defined joint and generation region parameters to display a 3-D view of the synthetic joints (left) and their traces along the cylinder wall (center). The joint intersection counts are displayed at the bottom right.

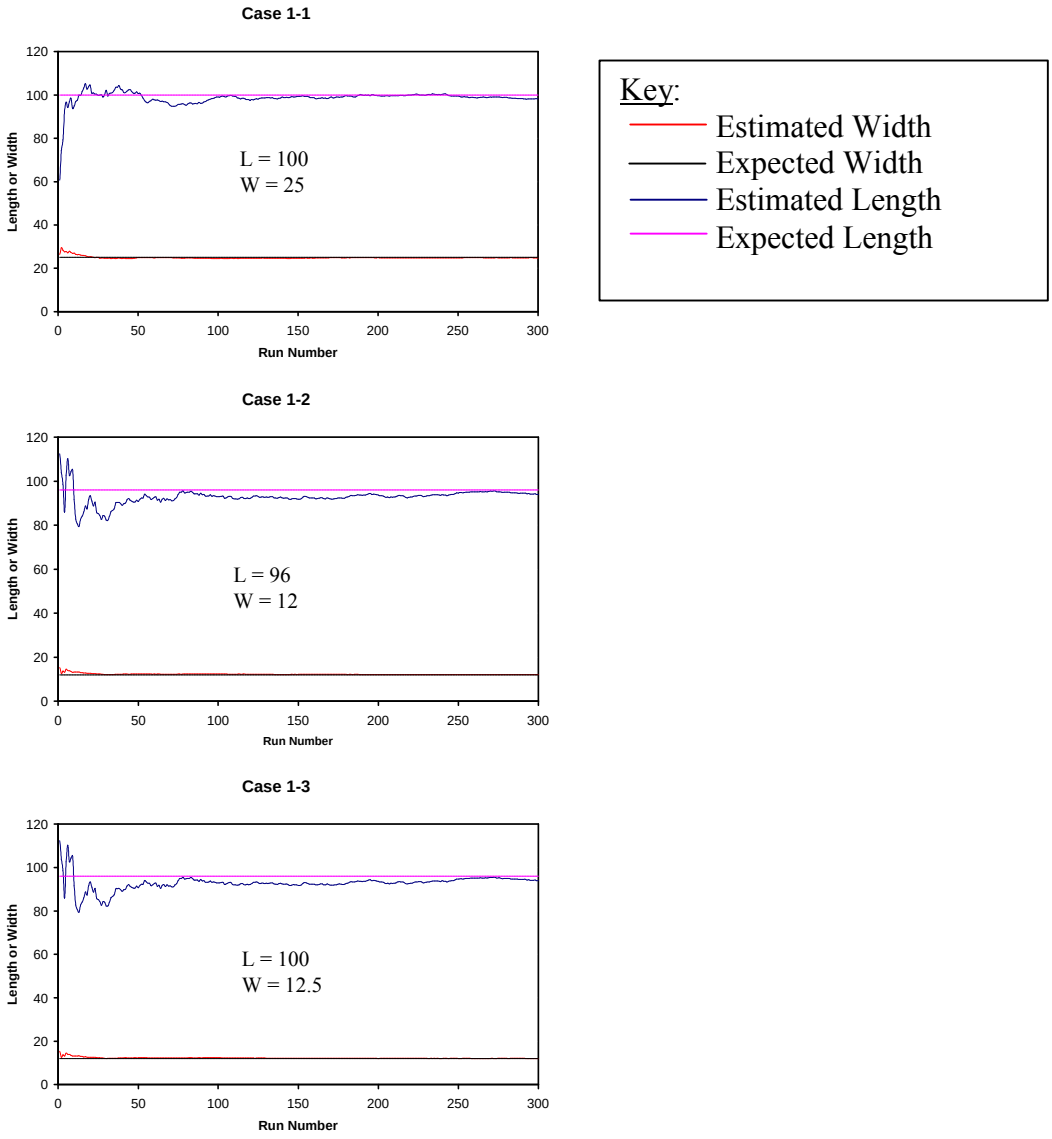


Figure 28. Estimator performance for Case 1 simulations. Plots show estimated value as a function of known value for an increasing number of runs.

Table 5. Case 1 simulation data along with length and width estimates to accompany Figure 28. (negative % error denotes underestimate)

Simulation Run	Number of Joints	Known				Estimated for 300 Runs				
		Fracture Length	**Fracture Width**	Aspect Ratio (L/W)	Intensity	Borehole Radius	**Fracture Length**	**Fracture Width**	% error L	% error W
Case 1-1	9311	100	25	4	1	3.125	98.22	24.84	-1.78	-0.63
Case 1-2	17731	96	12	8	1	1.5	94.01	12.08	-2.07	0.66
Case 1-3	17740	100	12.5	8	1	3.125	101.79	12.59	1.79	0.72

Case 2

Three simulations of 100 runs were performed where W'<D (Figure 29, Table 6). Joints were assumed to be normal to the borehole axis so that W'=W (Equation 1), and Equation 18 was used to estimate mean fracture length. For a single run, the average number of intersections counts are $\widetilde{N}_B$: 147, $\widetilde{N}_{B1}$: 57, $\widetilde{N}_{B2}$: 2, $\widetilde{N}_{B3}$: 78, and $\widetilde{N}_C$: 67, which typically yield estimates with an average variance of 12.1 from the expected lengths. Like the Case 1 simulations, as the runs accumulated for each simulation, the estimates tended to within 6% of the expected values (Figure 29, Table 6), demonstrating that the Case 2 estimators can accurately predict L.

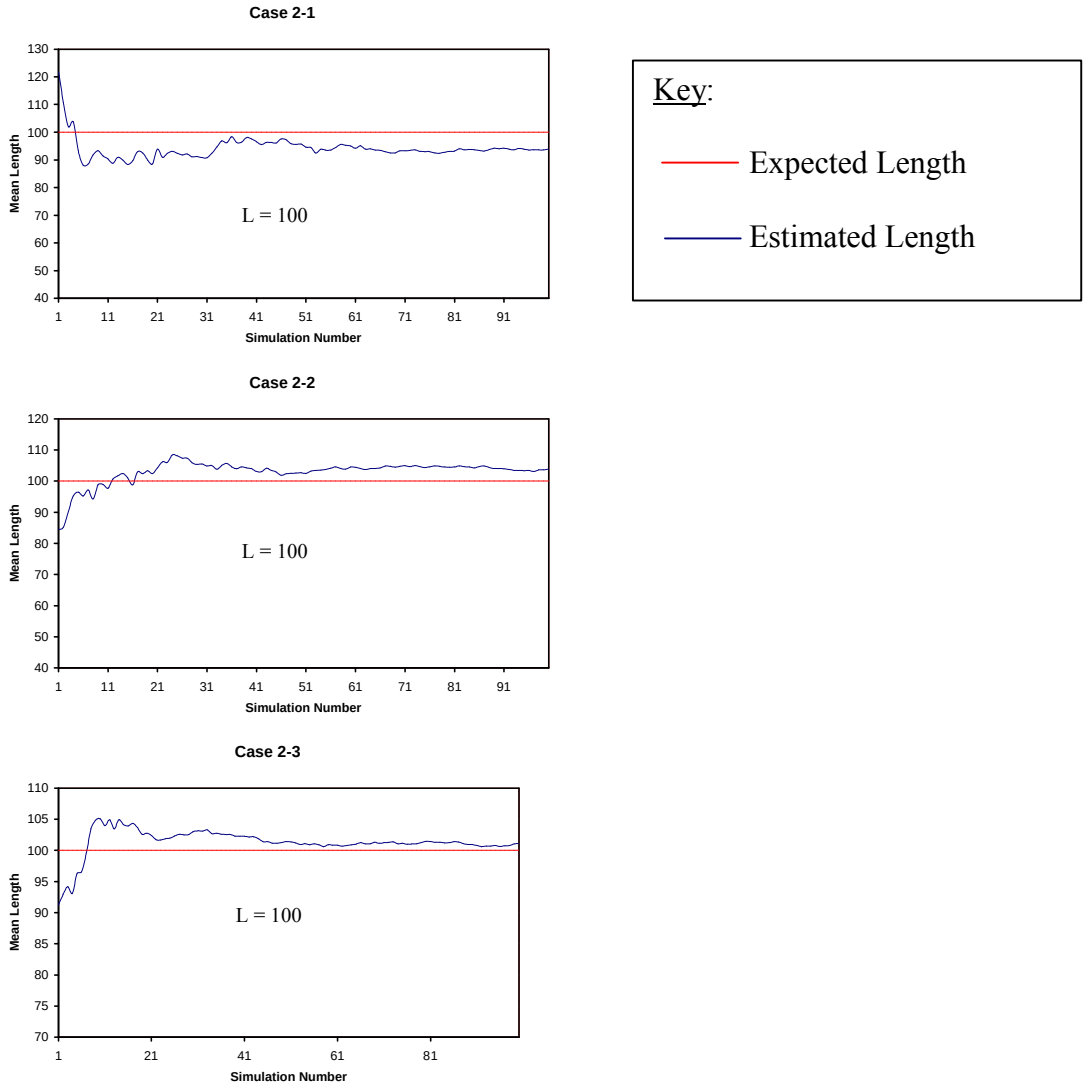


Figure 29. Estimator performance for Case 2 simulations. Plots show estimated L value as a function of known L-value for an increasing number of runs.

Table 6. Case 2 simulation data (negative % error denotes underestimate)

Simulation Run	Number of Joints	Known					Estimated for 100 Runs			
		Fracture Length	**Fracture Width**	Aspect Ratio (L/W)	Intensity	Borehole Radius	**Fracture Length**	**Fracture Width**	% error L	% error W
Case 2-1	10398	100	10	10	0.5	10	93.9	10.0	-6.11	0.00
Case 2-2	9311	100	5	20	0.5	10	103.8	5.0	3.83	0.00
Case 2-3	17731	100	10	10	0.5	20	101.1	10.0	1.11	0.00

V. SUBSURFACE JOINT ANALYSIS

All six wells sampled from the Piceance Creek area of the Piceance basin (Figure 13) contain A- and C-intersections. Based on the success of the Case 1 and 2 estimators, the Case 3 estimators were used to yield mean joint size estimates. Mean joint size was estimated for the joint population of the entire Mesaverde Group sample, but to discriminate whether size is controlled by stratigraphic or lithologic factors, for each well, size was estimated for the Mesaverde Group, Williams Fork Formation, Iles Formation, all sandstones in each stratigraphic unit, and all shales in each unit. The estimates obtained from the sandstone intervals are directly comparable to the surface data since sandstone outcrops were the sampled lithology the surface.

Joint Orientations

The subsurface fractures are similar to the surface fracture in orientation (Figure 30). The surface fractures strike ~WNW-ESE (Figure 5), and the subsurface fractures strike ~NW-SE (Figure 30), which is parallel to the trend of the Piceance Creek dome (Figure 13) rather than the inferred Laramide maximum horizontal compression direction for the surface joints, suggesting a local paleostress deflection

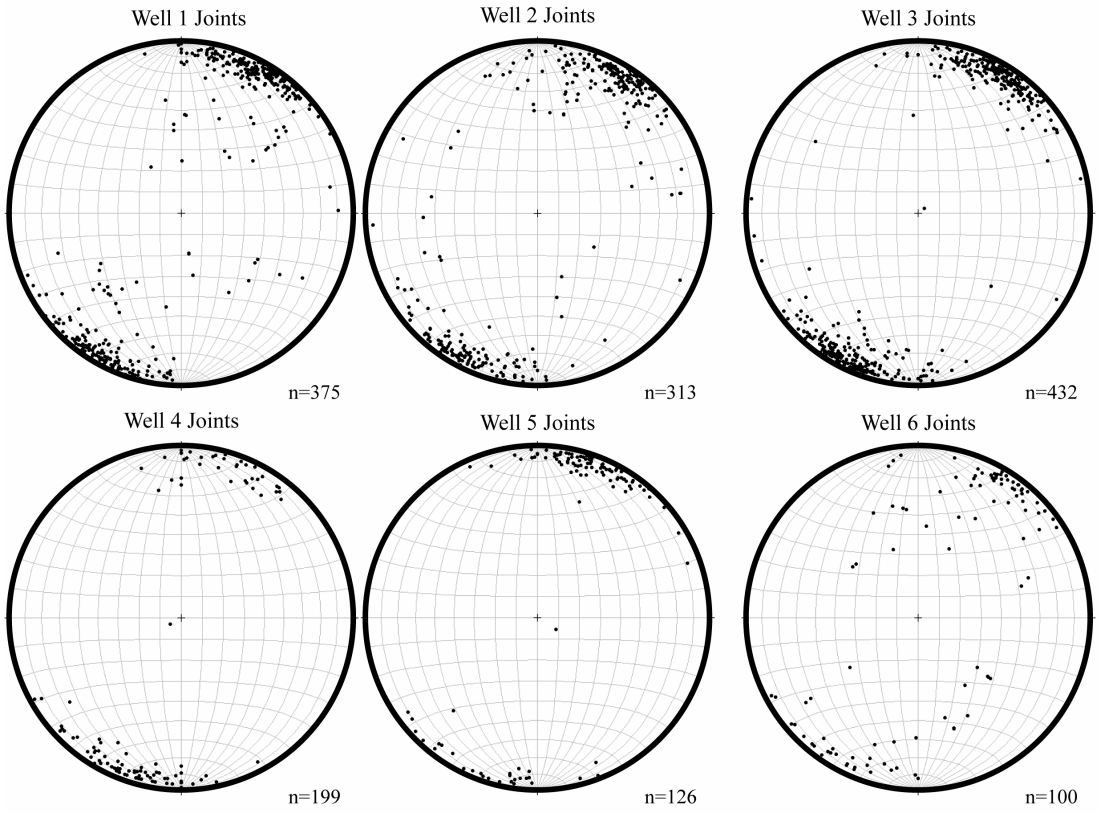


Figure 30. Equal-area stereonet plots of joint poles to bedding in all of the wells. A dominant NW-SE trend is noted for the joints, which is consistent with the surface geology. However, there is a lot of scatter within these plots, which is due to the mixing of fractures from another set and/or lower angle fractures that are possibly faults. Thus the master fracture set is filtered out for the analysis.

adjacent to this structure. However, some subsurface fractures deviate more than 25^0 from the normal to bedding (Figure 31), contributing much of the scatter in the stereoplots (Figure 30). The fractures are probably not bed-normal joints, so only fractures within 25^0 of the bedding normal as with surface joints are included (Figures 11, 31, 32)

Joints by Formation

Using the Case 3 estimators, joints within the Mesaverde Group have a mean bed-parallel length range of 13 to 39 m (43 to 127 ft) and a mean bed-perpendicular length range of 11 to 32 m (35 to 105 ft) (Table 7). Joints within the Williams Fork Formation have a mean bed-parallel length range of 14 to 42 m (47 to 138 ft) and a mean bed-perpendicular length range of 14 to 32 m (46 to 105 ft) (Table 7). Joints within the Iles Formation have a range of 6.6 to 23 m (22 to 75 ft) and 6.8 to 22 m (22 to 72 ft) for mean bed-parallel length and bed-perpendicular length, respectively (Table 7). Overall, the corresponding aspect ratios were close to one, ranging from 0.5 to 1.5, with 14 intervals having bed-parallel lengths greater than bed-perpendicular lengths as might be expected, and 14 intervals where bed-parallel lengths are less than bed-perpendicular lengths.

Joints by Lithology

Within the Mesaverde Group, the bed-parallel length and bed-perpendicular length estimates for the sandstone intervals range from 12 – 94 m (39 – 310 ft) and 15

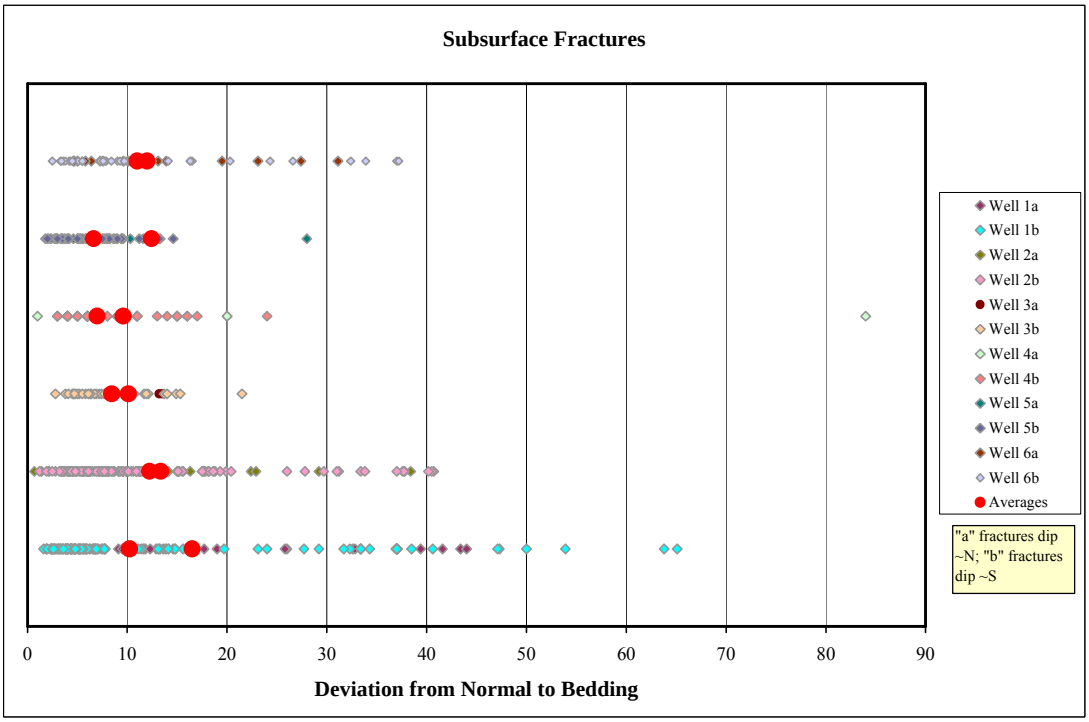


Figure 31. Plot of fracture dip deviation from normal to bedding for the subsurface fractures. A bed-normal fracture (dipping 90^0) will plot as 0^0 on this graph. As with the surface fractures, most of the fractures have a deviation of less than 20^0. The fractures that plot towards the right are assumed to be of a later fracture set that involved a different stress regime and thus are filtered out of the data set (Figure 32).

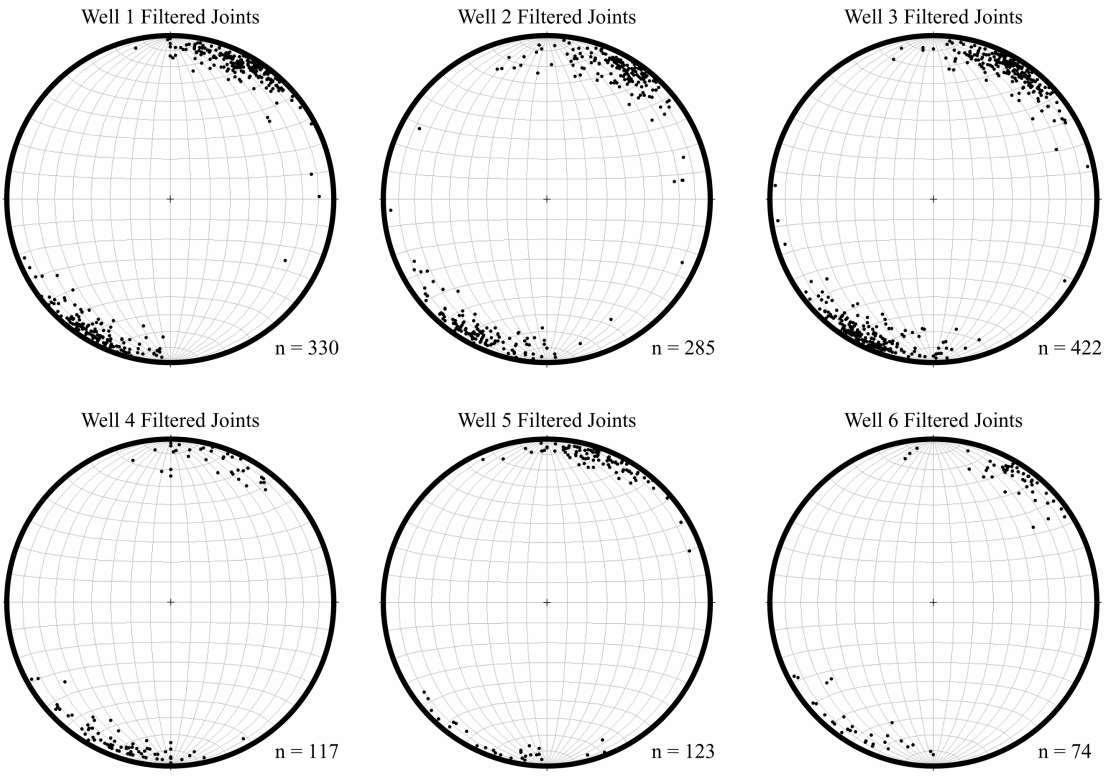


Figure 32. Equal-area stereonet plots showing all joints with dip greater than 65^0 (plot of poles to the plane). Surface data indicate that the master fracture set is approximately bed-normal, and thus the fractures that dip less than 65^0 are assumed to have a different origin than the master set. The filtered fractures shown are analyzed with the estimators.

Table 7. Intersection data and size estimates of subsurface fractures by stratigraphy (missing stratagraphic name indicates no data).

		Intersection Counts							Estimates						
Well	**Interval**	**A**	**B**	**B_1**	**B_2**	**B_3**	**C**	**Total Count**	**P_{32} (m^2/m^3)**	**P_{32} (ft^2/ft^3)**	**Bed-Parallel Length (m)**	**Bed-Parallel Length (ft)**	**Bed-Normal Length (m)**	**Bed-Normal Length (ft)**	**Aspect Ratio (L/W)**
1	Mesaverde Total	26	145	111	17	17	79	250	0.99	0.30	24.6	80.9	25.2	82.6	1.0
	WF Total	21	99	84	10	5	44	164	0.93	0.28	42.0	138.0	29.3	96.0	1.4
	Iles Total	5	46	27	7	12	35	86	1.54	0.47	13.4	43.9	21.9	71.9	0.6
2	Mesaverde Total	17	147	103	21	23	98	262	0.62	0.19	13.2	43.2	10.7	35.1	1.2
	WF Total	11	106	75	15	16	85	202	0.74	0.23	18.1	59.3	14.0	46.0	1.3
	Iles Total	6	41	28	6	7	13	60	0.51	0.15	6.6	21.7	6.8	22.2	1.0
3	Mesaverde Total	23	160	113	10	37	69	252	1.34	0.41	15.3	50.4	18.2	59.6	0.8
	WF Total	15	139	97	8	34	54	208	1.17	0.36	14.4	47.3	18.6	61.1	0.8
	Iles Total	8	21	16	2	3	15	44	2.60	0.79	16.9	55.6	11.5	37.7	1.5

Table 7. Continued

Well	Interval	Intersection Counts									Estimates				
		A	B	B_1	B_2	B_3	C	Total Count	P_{32} (m^2/m^3)	P_{32} (ft^2/ft^3)	Bed-Parallel Length (m)	Bed-Parallel Length (ft)	Bed-Normal Length (m)	Bed-Normal Length (ft)	Aspect Ratio (L/W)
4	Mesaverde Total	2	23	18	1	4	19	44	0.67	0.21	42.9	140.9	27.4	89.8	1.6
	WF Total	2	23	18	1	4	19	44	0.67	0.21	38.8	127.3	31.9	104.6	1.2
5	Mesaverde Total	18	55	35	4	16	52	125	0.42	0.13	18.3	59.9	19.4	63.5	0.9
	WF Total	11	28	14	3	11	28	67	0.40	0.12	15.8	51.8	29.5	96.8	0.5
	Iles Total	7	27	21	1	5	24	58	0.56	0.17	22.9	75.2	16.0	52.6	1.4
6	Mesaverde Total	9	44	33	2	9	20	73	0.30	0.09	22.1	72.5	19.8	65.1	1.1
	WF Total	4	38	29	2	7	17	59	0.28	0.09	24.6	80.6	20.5	67.3	1.2
	Iles Total	5	6	4	0	2	3	14	0.54	0.16	9.9	32.6	12.0	39.2	0.8

– 129 m (49 – 422 ft), while the bed-parallel length and bed-perpendicular length estimates for the shale intervals range 16 – 240 m (52 – 788 ft) and 8.1 – 76 m (27 – 249 ft), respectively (Table 8). The Williams Fork Formation sandstone bed-parallel length and bed-perpendicular length estimates range 16 – 89 m (53 – 290 ft) and 16 – 43 m (54 – 141 ft), and the shale interval bed-parallel length and bed-perpendicular length estimates range 19 – 53 m (63 – 174 ft) and 9.5 – 70 m (31 – 229 ft) (Table 8 indicates a maximum Williams Fork shale value of 465 m (1525 ft), but that is for only 1 intersection and is probably not that accurate), respectively. The Iles Formation sandstone bed-parallel length and bed-perpendicular length estimates range 3.5 – 79 m (12 – 258 ft) and 3.6 – 107 m (12 – 351 ft), and the shale bed-parallel length and bed-perpendicular length estimates ranged 7.6 – 19 m (25 – 63 ft) and 4.4 – 60 m (14 – 196 ft), respectively (Table 8). Overall, the aspect ratios tend to be small, ranging from 0.2 to 2.1, with 9 intervals having bed-parallel lengths greater than bed-perpendicular lengths, and 8 intervals where bed-parallel lengths are less than bed-perpendicular lengths.

Table 8. Intersection data and size estimates of subsurface fractures by lithology.

Well	Interval	Intersection Counts							Estimates						
		A	B	B_1	B_2	B_3	C	Total Count	P_{32} (m^2/m^3)	P_{32} (ft^2/ft^3)	Bed-Parallel Length (m)	Bed-Parallel Length (ft)	Bed-Normal Length (m)	Bed-Normal Length (ft)	Aspect Ratio (L/W)
1	Mesaverde Total	26	145	111	17	17	79	250	0.99	0.30	24.6	80.9	25.2	82.6	1.0
	Mesaverde Shales	1	7	7	0	0	10	18	0.27	0.08	n/a	n/a	29.4	96.6	n/a
	Mesaverde Sandstone	13	56	51	4	1	18	87	2.25	0.69	88.5	290.2	42.9	140.7	2.1
	WF Shales	1	7	7	0	0	10	18	0.27	0.08	n/a	n/a	29.4	96.6	n/a
	WF Sandstone	13	56	51	4	1	18	87	2.25	0.69	88.5	290.2	42.9	140.7	2.1
2	Mesaverde Total	17	147	103	21	23	98	262	0.62	0.19	13.1	43.0	10.6	34.9	1.2
	Mesaverde Shales	3	51	37	10	4	51	105	0.33	0.10	15.7	51.7	8.1	26.6	1.9
	Mesaverde Sandstone	14	85	57	10	18	35	134	1.38	0.42	11.9	39.2	15.0	49.1	0.8
	WF Shales	3	38	28	8	2	43	84	0.42	0.13	19.1	62.8	9.5	31.3	2.0
	WF Sandstone	7	55	38	5	12	30	92	1.56	0.47	16.4	53.9	17.7	58.1	0.9
	Iles Shale	0	13	9	2	2	8	21	0.33	0.10	7.6	25.0	4.4	14.4	1.7
	Iles Sandstone	7	30	19	5	6	5	42	0.72	0.22	3.5	11.3	5.7	18.7	0.6

Table 8. Continued.

Well	Interval	Intersection Counts							Estimates						
		A	B	B_1	B_2	B_3	C	Total Count	P_{32} (m^2/m^3)	P_{32} (ft^2/ft^3)	Bed-Parallel Length (m)	Bed-Parallel Length (ft)	Bed-Normal Length (m)	Bed-Normal Length (ft)	Aspect Ratio (L/W)
3	Mesaverde Total	24	163	115	11	37	69	256	1.34	0.41	15.0	49.4	18.0	59.2	0.8
	Mesaverde Shales	7	9	8	0	1	7	23	0.86	0.26	240.0	787.3	75.8	248.6	3.2
	Mesaverde Sandstones	4	16	11	2	3	10	30	4.17	1.27	94.4	309.9	128.7	422.3	0.7
	Iles Shale	7	9	8	0	1	7	23	1.46	0.45	190.2	624.1	59.8	196.2	3.2
	Iles Sandstone	4	16	11	2	3	10	30	4.63	1.41	78.7	258.2	106.9	350.8	0.7
4	WF Total	2	23	18	1	4	19	44	0.67	0.21	38.8	127.3	30.6	100.4	1.3
	WF Shales	0	4	3	0	1	2	6	0.38	0.12	52.9	173.7	69.8	228.9	0.8
	WF Sandstone	3	14	11	1	2	8	25	0.87	0.27	32.6	107.1	32.1	105.4	1.0

Table 8. Continued.

Well	Interval	Intersection Counts							Estimates						
		A	B	B_1	B_2	B_3	C	Total Count	P_{32} (m^2/m^3)	P_{32} (ft^2/ft^3)	Bed-Parallel Length (m)	Bed-Parallel Length (ft)	Bed-Normal Length (m)	Bed-Normal Length (ft)	Aspect Ratio (L/W)
5	Mesaverde Total	18	55	35	4	16	52	125	0.42	0.13	17.0	55.9	18.1	59.2	0.9
	Mesaverde Shales	0	5	2	2	1	2	7	0.12	0.04	17.2	56.4	73.2	240.3	0.2
	Mesaverde Sandstones	11	28	17	3	8	23	62	1.22	0.37	19.0	62.2	26.9	88.1	0.7
	WF Shales	0	1	1	0	0	0	1	0.07	0.02	n/a	n/a	464.9	1525.3	n/a
	WF Sandstone	6	13	7	2	4	14	33	1.35	0.41	31.7	103.9	42.5	139.4	0.7
	Iles Shale	0	4	1	2	1	2	6	0.35	0.11	8.1	26.5	37.2	122.1	0.2
	Iles Sandstone	5	15	10	1	4	9	29	0.46	0.14	3.5	11.6	3.6	11.7	1.0
6	Mesaverde Total	9	45	33	2	10	20	74	0.30	0.09	20.4	66.9	20.0	65.5	1.0
	Mesaverde Shales	0	4	4	0	0	0	4	0.08	0.02	n/a	n/a	36.8	120.9	n/a
	Mesaverde Sandstones	8	20	13	2	5	17	45	0.64	0.20	20.7	68.0	17.1	56.2	1.2
	WF Shales	0	4	4	0	0	0	4	0.08	0.02	n/a	n/a	36.8	120.8	n/a
	WF Sandstone	4	17	11	2	4	14	35	0.61	0.19	19.5	64.1	16.4	53.9	1.2
	Iles Sandstone	4	3	2	0	1	3	10	0.82	0.25	28.0	91.9	20.4	67.0	1.4

VI. DISCUSSION

Comparison of Subsurface and Surface Mean Size Estimates

Mean size estimates in the subsurface are much larger than those obtained from surface data. The smallest size estimates in the subsurface are equal to the largest measurements on the surface (ie. Well 5 - Iles Sandstone mean L and W (Table 8) vs. the L and W measurements in Tables 2 and 3). Additionally, joints measuring 240 m (787.4 ft) in length as within the Well 3 Mesaverde shales (Table 8) are absent at the surface. This difference in size may result from subsurface joint enhancement and/or misidentification of joints or intersections in the FMI logs.

Joint Enhancement

A potential explanation for the difference in magnitude of the surface and subsurface estimates is based on a geometric difference between surface and subsurface joints. Most, if not all, observed surface joints terminate at bedding surfaces (Figure 8), and thus, tend to be equal to or smaller than the bed thickness in height (~1-3 m, Table 2). However, between 10 to 25 % of the joints in wells 1-3 and 43 to 58 % in wells 4-6 cross bedding surfaces, which is much greater than on the surface (Figure 15, Table 9). Additionally, between 6 and 13 % of the joints have visible borehole-parallel heights greater than 3 m (Figure 15, Table 9), which is greater than the average penetration depth for the surface joints. Therefore, subsurface joints likely experienced a different deformation history than the surface joints due to some combination of greater driving stress, multiple stress events, greater bedding

Table 9. Percentage of subsurface joints occurring in single vs. mixed lithologies, or with borehole heights greater than 10 ft (~3 m).

Well	Single vs. Mixed Lithologies		% of Joints with Borehole Heights > 10 ft
	Single %	Mixed %	
1	75%	25%	13%
2	90%	10%	6%
3	90%	10%	8%
4	53%	47%	13%
5	42%	58%	11%
6	57%	43%	11%

surface contact strength, and/or differing elastic properties in the subsurface (Pollard and Aydin, 1988, Cooke and Underwood, 2001, Hoffmann et al., 2004).

One possible cause for the larger subsurface joints is increased fluid pressure created during gas generation. Gas generation began ~55 Ma and peaked between ~50 and 20 Ma (Yurewicz et al., 2003). Pressures related to gas generation would have only affected the present-day subsurface joints because the oldest joint set is dated prior to this event (~57 Ma) (Grout and Verbeek, 1992) and the basin rim uplift occurred prior to and during this event (middle to late Eocene, ~40-37 Ma) (Grout et al., 1991).

Another possibility for the difference between surface and subsurface size estimates is joint enhancement during drilling. Drilling-induced fractures form as a response to the interaction of drilling generated stresses with the present-day maximum horizontal stress direction. Rock failure is controlled by the magnitude and direction of the principal stresses (two horizontal, one vertical), and other mechanical properties such as rock strength, temperature, fluid pressures, and temperatures (Barton et al., 1998). For a vertical well, the drilling-generated stress will locally compose the vertical principal stress and the *in situ* horizontal maximum and minimum stresses compose the horizontal stresses. If the drilling-generated stress is large enough to cause rock failure (i.e. exceeds the yield stress), then a drilling-induced fracture will result parallel to the wellbore and the maximum horizontal stress direction (Barton et al., 1998). The master joint set strikes approximately parallel to the present-day maximum horizontal stress direction, which means the drilling

induced fractures, if they form, are parallel to these natural joints (Figure 33). Therefore, drilling-induced joint propagation could exploit the natural joints and link several smaller natural joints to create larger joints (Figure 34). This linking effect will enhance the bed-perpendicular lengths and likely bed-parallel lengths, leading to greater subsurface joint dimensions with respect to the surface.

Misidentification of Joint Traces/Intersections

While the joint traces and intersection identification is believed to be accurate, there is always potential sources of estimator error that are beyond control. These sources may cause the joints and or intersections to be misidentified, which in turn lead to estimator error. For example, natural joint traces may be enhanced by drilling-induced processes, and because drilling-induced fractures are parallel to the natural joints in these wells, the traces may be misidentified all together, such as calling a natural joint drilling induced, or vice versa. In this case, the intersection data set may include many induced fractures or exclude natural fractures, which will ultimately affect estimator performance. Additionally, image quality and resolution play an important part in the accuracy of joint trace identification. Poor image quality such as FMI tool pull, and features too small to be resolved all can lead to trace misidentification or even exclusion from the data set. The misidentification due to image quality will also lead to an over/under-count of the joint intersections, which will yield inaccurate size estimates.

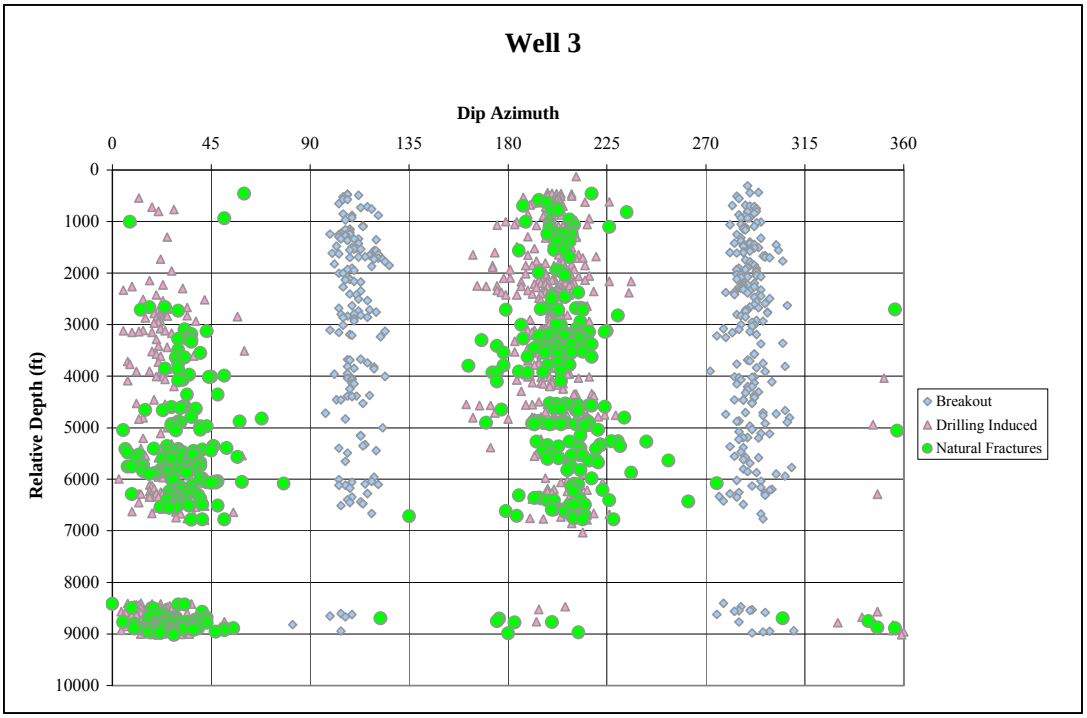


Figure 33. Graph of dip azimuth vs. depth for Well 3 (representative of all wells). The natural fracture trend (green circles) is parallel to the drilling induced trend (pink triangles), which indicates that the present-day maximum horizontal stress direction is parallel to the natural fracture trend.



Figure 34. Picture of a core showing the joint linkage. A drilling-induced fracture is present in the center of the core with a borehole height of 4.5 m (15+ ft) with part of the fracture lying out of the field of view. Closer examination of this core indicated that this drilling-induced fracture probably exploited several smaller natural fractures, causing one large fracture.

The joint intersection characteristics outlined previously (Table 4) usually hold true, although there are some in-between cases where the intersection type has to be interpreted. For example, in Figure 15 the B_1 intersection joint trace is not perfectly centered on the dip direction (or 90^0 from it), but it bears a strong resemblance to a B_1 intersection, rather than a B_3 intersection, and is thus labeled accordingly. Additionally, the FMI tool only covers ~70% of the borehole wall, and the no coverage zones (where a pad does not exist – Figure 14) are represented in the log by the absence of a borehole image (Figure 15). While the intersection counts are believed to be accurate in this study, there is always a possibility that some traces were misidentified, which could induce estimator error.

VII. CONCLUSIONS

1) Assuming an appropriate joint shape, borehole/joint intersections are classified and the relative abundance of each intersection type is proportional to the mean joint size.
2) Estimators are derived for three separate cases, which are defined based upon the size of the joint relative to the borehole. Simulation proves that the first two cases are accurate and valid for natural cases when the joints are known to definitively fall within a particular set of assumptions. The Case 3 estimators are derived from the already proven Case 1 and 2 mean size estimators, and are appropriate where the Case 1 or 2 assumptions are not satisfied.
3) Application of the Case 3 estimators to the Piceance basin well data yielded mean size estimates that were greater than those measured on the surface, but the estimated subsurface aspect ratios are consistent with those on the surface.
4) Possible sources of estimator error are speculated to be mainly joint enhancement, either by natural processes (gas generation) and/or by drilling processes (natural joint "linkage"). This source of error will lead to both misidentification of joint traces and intersection types, ultimately affecting estimator performance.

REFERENCES CITED

Amadei, B. and W.Z. Savage, 1993, Effects of joints on rock mass strength & deformability, *in* J.A. Hudson, Comprehensive Rock Engineering: New York, Pergamon, p. 331-365.

Barton, C.A., D.A. Castillo, D. Moos, P. Peska, and M.D. Zoback, 1998, Characterizing the full stress tensor based on observations of drilling induced wellbore failures in vertical and inclined boreholes leading to improved wellbore stability and permeability prediction: APPEA Journal, p. 466-488.

Barton, C.C., 1995, Fractal analysis of scaling and spatial clustering of fractures, *in* C.C. Barton and P.R. LaPointe, Fractals in the Earth Sciences: New York, Plenum Press, p. 141-178.

Barton, C.C., E. Larson, W.R. Page, and T.M. Howard, 1993, Characterizing fractured rock for fluid-flow, geomechanical, and paleostress modeling: Methods and preliminary results from Yucca Mountain, Nevada, USGS Open File Report, 93-269, 61 p.

Becker, A., and M.R. Gross, 1996, Mechanism for joint saturation in mechanically layered rocks: an example from southern Israel: Tectonophysics, v. 257, p. 223-237.

Brown, C. A., T.M. Smagala, and G.R. Haefele, 1986, Southern Piceance Basin Model: Cozzette, Corcoran and Rollins Sandstone, *in* C.W. Spencer, and R.F. Mast, Geology of tight gas reservoirs: Tulsa, American Association of Petroleum Geologists, v. 24, p. 207-219.

Cacas, M.C., E. Ledoux, G. de Marsily, and B. Tillie, 1989, The use of stochastic concepts in modeling fracture flow, *in* G. Jousma, J. Bear, Y.Y. Haimes, and F. Walter, Groundwater Contamination: Use of Models in Decision-Making: Boston, Kluwer Academic Publishers. 435-443.

Carroll, C.J., 2003, Fractures in the Mesaverde Group at Somerset Coal Field, Delta and Gunnison Counties, Colorado, *in* K.M. Peterson, T.M. Olson, and D.S. Anderson, Piceance Basin 2003 Guidebook: Denver, Rocky Mountain Association of Geologists, 194-206.

Cooke, M.L. and C.A. Underwood, 2001, Fracture termination and step-over at bedding interfaces due to frictional slip and interface opening: Journal of Structural Geology, v. 14, p. 133-137.

Cumella, S.P. and D.B. Ostby, 2003, Geology of the Basin-Centered Gas Accumulation, Piceance Basin, Colorado, *in* K.M. Peterson, T.M. Olson, and D.S. Anderson, Piceance Basin 2003 Guidebook: Denver, Rocky Mountain Association of Geologists, 171-193.

Dershowitz, W.S. and H.H. Einstein, 1988. Characterizing rock joint geometry with joint system models: Rock Mechanics and Rock Engineering, v. 21, p. 21-51.

Engelder, T., 1985, Loading paths to joint propagation during a tectonic cycle; an example from the Appalachian Plateau, U.S.A.: Journal of Structural Geology, v. 7, p. 459-476.

Engelder, T., 1987, Joints and shear fractures in rock, *in* B.K. Atkinson, Fracture Mechanics of Rock: London, Academic Press, p. 27-69.

Engelder, T., and M.P. Fischer, 1996, Loading configurations and driving mechanisms for joints based on the Griffith energy-balance concept: Tectonophysics, v. 25, p. 253-277.

Finely, S.J., and J.C. Lorenz, 1989, Characterization of natural fractures in Mesaverde reservoirs at the Multiwell Experiment site: Society of Petroleum Engineers Paper 19007, Society of Petroleum Engineers Joint Rocky Mountain Regional Meeting and Low-Permeability Reservoir Symposium, P. 721-728.

Franczyk, K.J., T.D. Fouch, R.C. Johnson, C.M. Molenaar, and W.A. Cobban, 1992, Cretaceous and Tertiary paleogeographic reconstructions for the Uinta-Piceance Basin study area, Colorado and Utah: U.S. Geological Society Bulletin, v. 1787-Q, p. Q1-Q37.

Gillespie, P.A., J.J. Walsh, J. Watterson, C.G. Bonson, and T. Manzocchi, 2001, Scaling relationship of joint and vein arrays from The Burren Co., Co. Claire, Ireland: Journal of Structural Geology, v. 23, p. 183-201.

Grout, M.A., G.A. Abrams, R.L. Tang, T.J. Hainsworth, and E.R. Verbeek, 1991, Late Laramide thrust related and evaporate-domed anticlines in the southern Piceance Basin, northeastern Colorado Plateau: AAPG Bulletin, v. 75, p. 205-218.

Grout, M.A. and E.R. Verbeek, 1992, Fracture history of the Divide Creek and Wolf Creek anticlines and its relation to Laramide basin-margin tectonism, southern Piceance Basin, northwestern Colorado: U.S. Geological Survey Bulletin, v. 1787-Z, 32 p.

Hoffmann, W., W.M. Dunne, and M. Mauldon, 2004, Probabilistic-mechanistic simulation of bed-normal joint patterns, *in* J.W. Cosgrove and T. Engelder, The Initiation, Propagation, and Arrest of Joints and Other Fractures: London, The Geological Society of London, Special Publications, v. 231, in press.

Johnson, S.Y., 1992. Phanerozoic evolution of sedimentary basins in the Uinta-Piceance Basin region, Northwestern Colorado and Northeastern Utah: U.S. Geological Survey Bulletin, v. 1787-F, p. F1-F38.

Johnson, R.C. and Flores, R.M., 2003. History of the Piceance Basin from the Latest Cretaceous Through Early Eocene and the Characterization of Lower Tertiary Sandstone Reservoirs, *in* K.M. Peterson, T.M. Olson, and D.S. Anderson, Piceance Basin 2003 Guidebook: Denver, Rocky Mountain Association of Geologists, 21-61.

LaPointe, P.R., and J.A. Hudson, 1985, Characterization and interpretation of rock mass joint patterns: Geological Society of America Special Paper, v. 199, 37 p.

Law, B.E., 2002, Basin-centered gas systems: AAPG Bulletin, v. 86, p. 1891-1919.

Lorenz, J. C., and S. J. Finley, 1991, Regional fractures II: Fracturing of Mesaverde reservoirs in the Piceance Basin, Colorado: AAPG Bulletin, v. 75, p. 1738-1757.

Lorenz, J.C., and R.E. Hill, 1994, Subsurface fracture spacing: comparison of inferences from slant/horizontal and vertical cores: Society of Petroleum Engineers Formation Evaluation, March, p. 66-72.

Mauldon, M., 1998, Estimating mean fracture trace length and density from observations in convex windows: Rock Mechanics and Rock Engineering, v. 31, p. 201-216.

Mauldon, M., W. M. Dunne, and M.B. Rohrbaugh Jr., 2001, Circular scanlines and circular windows: New tools for characterizing the geometry of fracture traces: Journal of Structural Geology, v. 23, p. 247-258.

Mauldon, M., M.B. Rohrbaugh, Jr., W.M. Dunne, and W. Lawdermilk, W., 1999, Estimators for mean fracture trace length and density using circular window, *in* B. Amadei, R.L. Kranz, G.A. Scott, P.H. Smeallie, Proceedings of the 37th US Rock Mechanics Symposium - Rock Mechanics for Industry: Rotterdam, Balkema, p. 785-792.

Mauldon, M., and X. Wang, 2003, Measuring fracture intensity in tunnels using cycloidal scanlines, in Culligan, Einstein and Whittle, Proceedings from the 12th Pan-American Conference on Soil Mechanics and Geotechnical Engineering and the 39th U.S. Rock Mechanics Symposium Soil and Rock America 2003: v. 1, p. 123-128.

Narr, W., 1996, Estimating Average Fracture Spacing in Subsurface Rock: AAPG Bulletin, v. 80, no. 10, p. 1565-1586.

Odling, N.E., 1997, Scaling and connectivity of joint systems in sandstones from western Norway: Journal of Structural Geology v. 19, p. 1257-1271.

Patterson, P.E., K. Kronmueller, T.D. Davies, 2003, Sequence Stratigraphy of the Mesaverde Group and Ohio Creek Conglomerate, Northern Piceance Basin,

Colorado, *in* K.M. Peterson, T.M. Olson, and D.S. Anderson, Piceance Basin 2003 Guidebook: Denver, Rocky Mountain Association of Geologists, p. 115-129.

Pollard, D.D., and A. Aydin, 1988, Progress in understanding jointing over the past century: Geological Society of America Bulletin, v. 100, p. 1181-1204.

Priest, S.D. and J.A. Hudson, 1981, Estimation of discontinuity spacing and tracelength using scanline surveys. International Journal of Rock Mechanics and Mining Sciences and Geomechanics Abstracts, v. 18, p. 183-197.

Rohrbaugh, M.B., M. Mauldon, and W.M. Dunne, 2002, Estimating fracture trace intensity, density, and mean length using circular scanlines and windows: AAPG Bulletin, v. 86, p. 2089-2104.

Sclumberger, 2002, FMI: Borehole geology, geomechanics, 3D reservoir modeling, <http://www.oilfield.slb.com/media/services/formation/geology/fmi.pdf?>, Accessed September 29, 2003.

Thorp, R.K., B.J. Watkins, W.E. Ralph, 1983, Strength and permeability of an ultra-large specimen of granitic rock, *in* C.C. Mathewson, Rock Mechanics Theory – Experiment – Practice, Proceedings of the 24th US Rock Mechanics Symposium: Collage Station, Texas A&M University Press, p. 511-518.

Verbeek, E.R. and M.A. Grout, 1998, Relation Between Basement Structures and Fracture Systems in Cover Rocks, Northeastern and Southwestern Colorado Plateau: U.S. Geological Survey Bulletin, v. 2158, p. 111-149.

Wang, X., M. Mauldon, W. M. Dunne, and C. Heiny, 2004, Using borehole data to estimate size and aspect ratio of subsurface fractures, Proceedings of Gulf Rocks 2004, 6th North American Rock Mechanics Symposium (NARMS), Houston.

Witherspoon, P.A., C.H. Amick, J.E. Gale, and K. Iwai, 1979, Observations of a potential size effect in experimental determination of the hydraulic properties of fractures: Water Resources Research, v. 15, p. 1142.

Wu, H. and D.D. Pollard, 1995, An experimental study of the relationship between joint spacing and layer thickness: Journal of Structural Geology, v. 17, p. 887-905.

Yurewicz, D.A., K.M. Bohacs, J.D. Yeakel, and K. Kronmueller, 2003, Source rock analysis and hydrocarbon generation, Mesaverde Group and Mancos Shale, Northern Piceance Basin, Colorado, *in* K.M. Peterson, T.M. Olson, and D.S. Anderson Piceance Basin 2003 Guidebook: Denver, Rocky Mountain Association of Geologists, p. 130-153.

APPENDICES

APPENDIX A

CASE 1 ESTIMATOR DERIVATION

Two equations for estimating L and W are based on the ratio of $\frac{\tilde{N}_{B1}}{\tilde{N}_{B2}}$ (Equation 14, or A-1) and ratio of B intersections to A intersections, $\frac{\tilde{N}_{A}}{\tilde{N}_{B}}$ (Equation 13, or A-2). These two simultaneous equations are needed to solve for the two unknowns L and W.

$$\frac{\tilde{N}_{A}}{\tilde{N}_{B}} = \frac{2(\mathrm{L} + \mathrm{W}')\mathrm{D} - \mathrm{D}^2 + p\frac{\mathrm{D}^2}{4}}{(\mathrm{W}'-\mathrm{D})(\mathrm{L}-\mathrm{D})} \tag{A-1}$$

$$\frac{\tilde{N}_{B1}}{\tilde{N}_{B2}} = \frac{2(\mathrm{L}-\mathrm{D})\mathrm{D} + \mathrm{D}^2 - \pi\frac{\mathrm{D}^2}{4}}{2(\mathrm{W}'-\mathrm{D})\mathrm{D} + \mathrm{D}^2 - \pi\frac{\mathrm{D}^2}{4}} \tag{A-2}$$

The overall method is to rewrite the N_{B1}/N_{B2} equation in terms of L, substitute L in Equation A-1, and solve the equation for W' as quadratic roots of the equation. Then the W'-values may be substituted into Equation A-2 to obtain L. Thus, the first step in rewriting Equation A-2 for L is to expand the right side:

$$\frac{\tilde{N}_{B1}}{\tilde{N}_{B2}} = \frac{2\mathrm{DL} - 2\mathrm{D}^2 + \mathrm{D}^2 - \pi\frac{\mathrm{D}^2}{4}}{2\mathrm{DW}'-2\mathrm{D}^2 + \mathrm{D}^2 - \pi\frac{\mathrm{D}^2}{4}} \tag{A-3a}$$

Combining terms, dividing through by D, and factoring leads to

$$\frac{\tilde{N}_{B1}}{\tilde{N}_{B2}} = \frac{2\text{L - D}\left(1+\frac{p}{4}\right)}{2\text{W'-D}\left(1+\frac{p}{4}\right)}. \qquad \text{(A-3b)}$$

Moving the right-side denominator to the left

$$2\frac{\tilde{N}_{B1}}{\tilde{N}_{B2}}W' - \frac{\tilde{N}_{B1}}{\tilde{N}_{B2}}D\left(1+\frac{p}{4}\right) = 2L - D\left(1+\frac{p}{4}\right). \qquad \text{(A-3c)}$$

Rearranging Equation A-3c so that L is on the left side

$$2L - D\left(1+\frac{p}{4}\right) = 2\frac{\tilde{N}_{B1}}{\tilde{N}_{B2}}W' - \frac{\tilde{N}_{B1}}{\tilde{N}_{B2}}D\left(1+\frac{p}{4}\right). \qquad \text{(A-3d)}$$

Simplifying the left side to yield only L,

$$L = \frac{2\frac{\tilde{N}_{B1}}{\tilde{N}_{B2}}W'}{2} - \frac{\frac{\tilde{N}_{B1}}{\tilde{N}_{B2}}D\left(1+\frac{p}{4}\right)}{2} + \frac{D\left(1+\frac{p}{4}\right)}{2}. \qquad \text{(A-3e)}$$

Factoring, A-3e becomes

$$L = \left(\frac{\tilde{N}_{B1}}{\tilde{N}_{B2}}\right)W' - \frac{\left(1+\frac{p}{4}\right)D}{2}\left(\frac{\tilde{N}_{B1}}{\tilde{N}_{B2}} - 1\right). \qquad \text{(A-3f)}$$

Solving the N_B/N_A Ratio

Substituting for L in Equation A-1 using Equation A-3f yields

$$\frac{\tilde{N}_A}{\tilde{N}_B} = \frac{2D\left[\left(\frac{\tilde{N}_{B1}}{\tilde{N}_{B2}}\right)W' - \frac{\left(1+\frac{p}{4}\right)D}{2}\left(\frac{\tilde{N}_{B1}}{\tilde{N}_{B2}} - 1\right) + W'\right] - D^2 + p\,\frac{D^2}{4}}{(W'-D)\left(\left(\frac{\tilde{N}_{B1}}{\tilde{N}_{B2}}\right)W' - \frac{\left(1+\frac{p}{4}\right)D}{2}\left(\frac{\tilde{N}_{B1}}{\tilde{N}_{B2}} - 1\right) - D\right)}. \qquad \text{(A-4)}$$

Solving for W' will yield a quadratic equation and thus Equation A-4 needs to be placed in the form of $ax^2 + bx + c = 0$ so that the quadratic roots may be determined. To simplify the derivation, variables are substituted for some terms:

$$v = \frac{\tilde{N}_A}{\tilde{N}_B}$$

$$x = \frac{\tilde{N}_{B1}}{\tilde{N}_{B2}}$$

y = (1+(π/4)),

yielding

$$v = \frac{2D\left(\left(xW' - \frac{Dx}{2}y + \frac{D}{2}y\right) + W'\right) - D^2 + p\,\frac{D^2}{4}}{(W' - D)\left(xW' - \frac{Dx}{2}y + \frac{D}{2}y - D\right)}. \qquad \text{(A-4a)}$$

First, the right-side top and bottom are expanded:

$$v = \frac{2DxW' - D^2xy + D^2y + 2DW' - D^2 + p\,\frac{D^2}{4}}{xW'^2 - \frac{Dxy}{2}W' + \frac{Dy}{2}W' - DW' - DxW' + \frac{D^2xy}{2} - \frac{D^2y}{2} + D^2}. \qquad \text{(A-4b)}$$

Moving the right-side denominator to the left and multiplying through by *v* yields:

$$vxW'^2 - \frac{Dvxy}{2}W' + \frac{Dvy}{2}W' - DvW' - DvxW' + \frac{D^2vxy}{2} - \frac{D^2vy}{2} + D^2v = 2DxW' - D^2xy + D^2y + 2DW' - D^2 + p\,\frac{D^2}{4} \qquad \text{(A-4c)}$$

Next, the right side terms are moved to the left and reorganized.

$$vxW'^2 - \left[\frac{Dvxy}{2} - \frac{Dvy}{2} + Dv + Dvx + 2Dx + 2D\right]W' + \frac{D^2vxy}{2} - \frac{D^2vy}{2} + D^2v + D^2xy - D^2y + D^2 - p\frac{D^2}{4} = 0 \quad \text{(A-4d)}$$

Equation A-4d is in the form of $a_wx^2+b_wx+c_w=0$, where x=W'. Thus, the a_w, b_w, and c_w-terms are:

$$a_w = vx = \left(\frac{\tilde{N}_{B1}}{\tilde{N}_{B2}}\right)\left(\frac{\tilde{N}_A}{\tilde{N}_B}\right) \quad \text{(A-5a)}$$

$$b_w = -D\left[\frac{vxy}{2} - \frac{vy}{2} + v + vx + 2x + 2\right] = -D\left[\frac{\tilde{N}_A}{\tilde{N}_B}\left(\frac{1+\frac{p}{4}}{2}\left(\frac{\tilde{N}_{B1}}{\tilde{N}_{B2}} - 1\right) + 1 + \frac{\tilde{N}_{B1}}{\tilde{N}_{B2}}\right) + 2\left(\frac{\tilde{N}_{B1}}{\tilde{N}_{B2}} + 1\right)\right] \quad \text{(A-5b)}$$

$$c_w = D^2\left[\frac{vxy}{2} - \frac{vy}{2} + v + xy - y + -\frac{p}{4}\right] = D^2\left[\frac{\tilde{N}_A}{\tilde{N}_B}\left(\frac{1+\frac{p}{4}}{2}\left(\frac{\tilde{N}_{B1}}{\tilde{N}_{B2}} - 1\right) + 1\right) + \left(1+\frac{p}{4}\right)\left(\frac{\tilde{N}_{B1}}{\tilde{N}_{B2}} - 1\right) + 1 - \frac{p}{4}\right] \quad \text{(A-5c)}$$

The above terms are substituted into the quadratic roots formula.

$$W' = \frac{-b_w \pm \sqrt{b_w^2 - 4(a_w)(c_w)}}{2a_w} \tag{A-6}$$

Typically only one real root exists and that is the value for W'. The mean W' estimate is then substituted into Equation A-3f to obtain mean L. True mean W is calculated by dividing W' by the cosine of the fracture dip.

Using the quadratic to solve for L (Opposite order from above)

Rewriting Equation A-2 in terms of W instead of L yields:

$$W' = \left(\frac{\tilde{N}_{B_2}}{\tilde{N}_{B_1}}\right)L - \frac{\left(1+\frac{p}{4}\right)D}{2}\left(\frac{\tilde{N}_{B_2}}{\tilde{N}_{B_1}} - 1\right). \tag{A-7}$$

The steps for determining the coefficients (a_l, b_l, and c_l) of the resultant quadratic equation in terms of L are the same as above, except N_{B1}/N_{B2} is inverted and *W'* is substituted for *L*. Thus, the resulting coefficients for the quadratic roots equation are defined as:

$$a_l = \left(\frac{\tilde{N}_{B_2}}{\tilde{N}_{B_1}}\right)\left(\frac{\tilde{N}_B}{\tilde{N}_A}\right), \tag{A-8a}$$

$$b_l = -D\left[\frac{\tilde{\tilde{N}}_B}{\tilde{\tilde{N}}_A}\left(\frac{1+\frac{p}{4}}{2}\left(\frac{\tilde{\tilde{N}}_{B_2}}{\tilde{\tilde{N}}_{B_1}}-1\right)+1+\frac{\tilde{\tilde{N}}_{B_2}}{\tilde{\tilde{N}}_{B_1}}\right)+2\left(\frac{\tilde{\tilde{N}}_{B_2}}{\tilde{\tilde{N}}_{B_1}}+1\right)\right], \tag{A-8b}$$

$$c_l = D^2\left[\frac{\tilde{\tilde{N}}_B}{\tilde{\tilde{N}}_A}\left(\frac{1+\frac{p}{4}}{2}\left(\frac{\tilde{\tilde{N}}_{B_2}}{\tilde{\tilde{N}}_{B_1}}-1\right)+1\right)+\left(1+\frac{p}{4}\right)\left(\frac{\tilde{\tilde{N}}_{B_2}}{\tilde{\tilde{N}}_{B_1}}-1\right)+1-\frac{p}{4}\right]. \tag{A-8c}$$

APPENDIX B

CASE 3 ESTIMATOR DERIVATION

The following derivation is credited to Wang and Mauldon, personal communication.

Assumptions for the derivation:

1. The aspect ratio α of fractures is constant, so

   $L = \alpha W'$, and

   $E(L) = \alpha E(W')$, or $\mu_L = \alpha \mu_{W'}$,

   where E(.) and *m* are the expected values.

2. The length and width of fractures have distributions of L ~ $f_L(l)$ and W ~ $f_{w'}$(w') with mean and variance of (μ_L, σ_L^2) and $(\mu_{W'}, \sigma_{W'}^2)$ respectively. (Figure B-1)

3. Only case 1 (W' > D) and case 2 (W' < D, L > D) are involved in the derivation.

Let N_{B1}, N_{B2}, N_{B3}, N_{B4}, N_C, N_A be random variables. Let $\tilde{N}_{B1}$, $\tilde{N}_{B2}$, $\tilde{N}_{B3}$, $\tilde{N}_{B4}$, $\tilde{N}_C$ and $\tilde{N}_A$ denote the sample values (observed number of occurrences) of intersection type B_1, B_2, B_3, B_4, C and A, respectively. Let B denote all B-type intersections and $\tilde{N}_B$ denote the sample values of all type B intersections.

For case 1, W > D (Figure 21), the expected value of N_A can be expressed as

$$E(N_A) = \int_{aD}^{\infty} E(N_A \mid l)\, f_L(l)\, dl \,, \qquad \text{(B-1)}$$

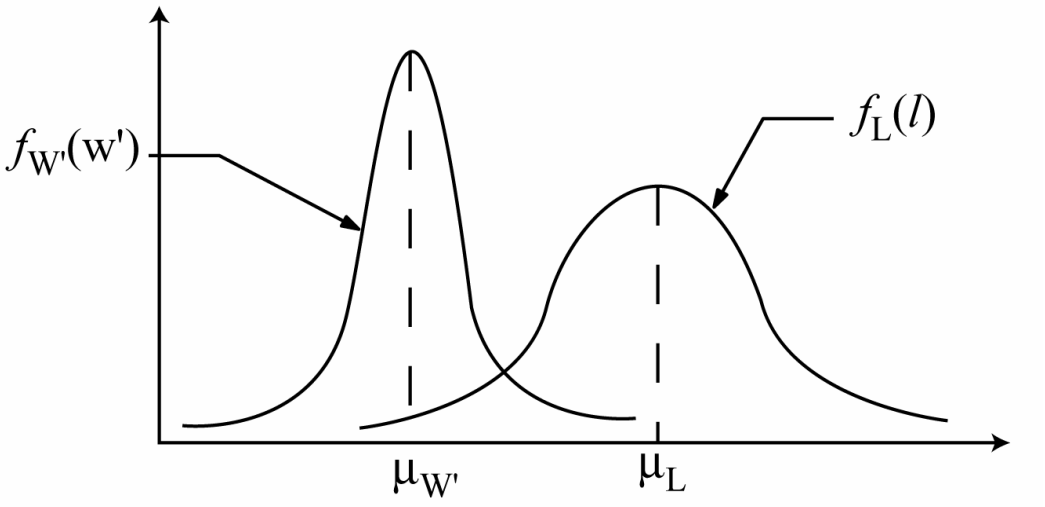


Figure B-1: Illustration of the pdf's of the L and W' of the fractures. Each has a distribution, *f*, about the mean *m*. Although a normal distribution is shown here, the equations size estimator equations are distribution free. The borehole diameter, D, can fall anywhere on the x-axis, and thus the distributions and resulting estimators are not dependent on its size (from Wang and Mauldon, personal communication).

where $E(N_A \mid l)$ is the expected value of A type intersections for a given *l*. It is proportional to the area of the A-intersection area (Appendix A), and Equation (B-1) can be written as

$$E(N_A) = \int_{\alpha D}^{\infty} \lambda(w'-D)(l-D) f_L(l) dl = \lambda \int_{\alpha D}^{\infty} (l/\alpha - D)(l-D) f_L(l) dl \,, \qquad \text{(B-2)}$$

where λ is a constant factor.

For case 2 (Figure 22), W' < D, L > D, the expected value of N_C can be expressed as

$$E(N_C) = \int_{0}^{aD} E(N_C \mid l) f_L(l) dl \,, \qquad \text{(B-3)}$$

where $E(N_C \mid l)$ is the expected value of C-intersections for a given *l*. It is proportional to the C-intersection area. Then the above equation can be written as

$$E(N_C) = \int_{0}^{\alpha D} -\lambda(w'-D)(l-D) f_L(l) dl = -\lambda \int_{0}^{\alpha D} (l/\alpha - D)(l-D) f_L(l) dl \,. \qquad \text{(B-4)}$$

Subtracting Equation (B-4) from Equation (B-2) yields:

$$E(N_A) - E(N_C) = \lambda \int_{\alpha D}^{\infty} (l/\alpha - D)(l - D) f_L(l) dl + \lambda \int_{0}^{\alpha D} (l/\alpha - D)(l - D) f_L(l) dl$$

$$= \lambda \int_{0}^{\infty} (l/\alpha - D)(l - D) f_L(l) dl \qquad \text{(B-5)}$$

$$= \lambda \left[E[l^2]/\alpha - D(1/\alpha + 1)\mu_L + D^2 \right]$$

Similarly (see notes), we will get

$$E(N_{B1}) + 2E(N_C) = l\left[2Dm_L - (1 + p/4)D^2\right], \text{ and} \qquad \text{(B-6)}$$

$$E(N_B) - E(N_{B1}) = l\left[2Dm_W + pD^2/2\right]. \qquad \text{(B-7)}$$

$$^{*}\ E(all) = l\left[s_L^2/a + D(1 + 1/a)m_L + pD^2/4\right]$$

Dividing equation B-6 by B-7 yields:

$$\frac{E(N_{B1}) + 2E(N_C)}{E(N_B) - E(N_{B1})} = \frac{\lambda[2D\mu_L - (1 + \pi/4)D^2]}{\lambda[2D\mu_{W'} + \pi D^2/2]}, \text{ which yields}$$

$$\frac{E(N_{B1}) + 2E(N_C)}{E(N_B) - E(N_{B1})} = \frac{4\mu_L - (2 + \pi/2)D}{4\mu_{W'} + \pi D}. \qquad \text{(B-8)}$$

Three independent equations (B-5), (B-6), and (B-7) have five unknown variables: λ, α, μ_W, μ_L and $E[l^2]$, in which $\mu_{W'}$ and μ_L are related by

$$\mu_L = \alpha\mu_{W'} \qquad \text{(B-9)}$$

E[l^2] is related to variance of l, s_L^2, by

$$E[l^2] = \sigma_L^2 + \mu_l^2 \tag{B-10}$$

Estimation of λ

λ is assumed to be constant in this derivation. The derivation below provides a way to estimate λ.

From stereology,

$$P_{32} = S_V = N_V \langle A_F \rangle , \tag{B-11}$$

where S_V or P_{32} is the volumetric intensity of fractures (defined as fracture surface area per unit volume – Appendix C); N_V is the number of fractures per unit volume, and $<A_F>$ is the mean surface area of fractures.

Since λ is the number of fractures per unit area, it can also be expressed as

$$\lambda = N_V H , \tag{B-12}$$

where H is the height of sample borehole. Then Equation (B-11) is written as

$$P_{32} = \frac{l}{H}\left\langle A_F \right\rangle, \tag{B-13}$$

from which we obtain the estimate of λ:

$$\lambda = \frac{HP_{32}}{\left\langle A_F \right\rangle}. \tag{B-14}$$

The expected value of rectangular fracture surface area can be estimated as

$$\left\langle A_F \right\rangle \approx \mu_L \mu_{W'}. \tag{B-15}$$

Substitution of (B-15) into (B-14) yields:

$$\lambda = \frac{HP_{32}}{\mu_L \mu_{W'}}. \tag{B-16}$$

Estimators for m_W and m_L

Substitution of equation (B-16) into equations (B-6), (B-7), and (B-8), the following quadratic equation is obtained.

$$a_{W'}\mu_{W'}^{\,2} + b_{W'}\mu_{W'} + c_{W'} = 0 \tag{B-17}$$

Then the mean fracture width is estimated by

$$\mu_{W'} = \frac{-b_{W'} + \sqrt{b_{W'}^2 - 4a_{W'}c_{W'}}}{2a_{W'}}, \tag{B-18}$$

where

$$a_{W'} = \widetilde{N}_{B1} + 2\widetilde{N}_C, \tag{B-19}$$

$$b_{W'} = \pi\left(\widetilde{N}_{B1} + 2\widetilde{N}_C\right)\frac{D}{4} + \left(\widetilde{N}_B - \widetilde{N}_{B1}\right)(4+\pi)\frac{D}{8} - 2HP_{32}D, \tag{B-20}$$

$$c_{W'} = \frac{-\pi HP_{32}D^2}{2}, \tag{B-21}$$

From equation (B-8), the mean fracture length is estimated by

$$\mu_L = \frac{\widetilde{N}_{B1} + 2\widetilde{N}_C}{\widetilde{N}_B - \widetilde{N}_{B1}}\left(\mu_{W'} + \pi D/4\right) + (4+\pi)D/8. \tag{B-22}$$

Notes to Appendix B

Let $E(all)$ denote the expected number of intersections of all types. It is expressed as

$$\begin{aligned} E(all) &= \int_0^\infty \lambda(\Delta_A + \Delta_C + \Delta_B) f_L(l) dl \\ &= \lambda \int_0^\infty \left[(l/\alpha + D)(l + D) - D^2(1 - \pi/4) \right] f_L(l) dl \\ &= \lambda \left[E[l^2]/\alpha + D(1/\alpha + 1)\mu_L + D^2\pi/4 \right]. \end{aligned} \tag{B-23}$$

Similarly, denote $E(N_B) - \mathrm{E}(N_{B1})$ the expected number of intersections of all B-intersections except B_1.

$$\begin{aligned} E(N_B) - E(N_{B_1}) &= \int_0^\infty \lambda(Area_{B2} + Area_{B3} + Area_{B4}) f_L(l) dl \\ &= \lambda \int_0^\infty \left[2W'D + D^2\pi/2 \right] f_L(l) dl \\ &= \lambda \left[2\mu_{W'}D + D^2\pi/2 \right]. \end{aligned} \tag{B-24}$$

Comparing equation (B-5) to equations (B-23) and (B-24) yields:

$$E(all) - \left(E(N_A) - E(N_C)\right) - \left(E(N_B) - E(N_{B1})\right) = E(N_{B1}) + 2E(N_C)$$

$$= \lambda\left[2D\mu_L - (1+\pi/4)D^2\right]. \qquad \text{(B-25)}$$

APPENDIX C

P_{32} DETERMINATION FROM CYCLOIDAL SCANLINES AND DATA FROM THE MESAVERDE GROUP, PICEANCE BASIN, CO

Mauldon and Wang (2003) developed a procedure to estimate volumetric fracture intensity, P_{32}, for fractures that intersect a cylinder. This is accomplished by using cycloidal scanlines. A cycloid is defined as the locus of a point (P) on a the rim of a circle of radius (R) rolling along a straight line (x') of length = pd (d=generator circle diameter) (Figure C-1), and satisfies the following equations:

$$x' = r(\alpha - \sin\alpha) \tag{C-1}$$

$$z' = r(1 - \cos\alpha), \tag{C-2}$$

where *a* is the angle of rotation of the circle.

The cycloid is then deployed onto the borehole, or in this case the borehole image, where the fracture/scanline intersections are counted (Figure C-2). This procedure is repeated at regularly spaced, predefined intervals where the intersection counts and the scanline length are summed (Figure C-2). This intersection count to scanline length ratio provides a measure of linear intensity or P_{10}. The volumetric intensity is thus estimated by

$$P_{32} = 2P_{10} = 2\left(\frac{N}{xl}\right), \tag{C-3}$$

where N is the total intersection counts, *l* is the scanline length, and *x* is the total number of scanlines.

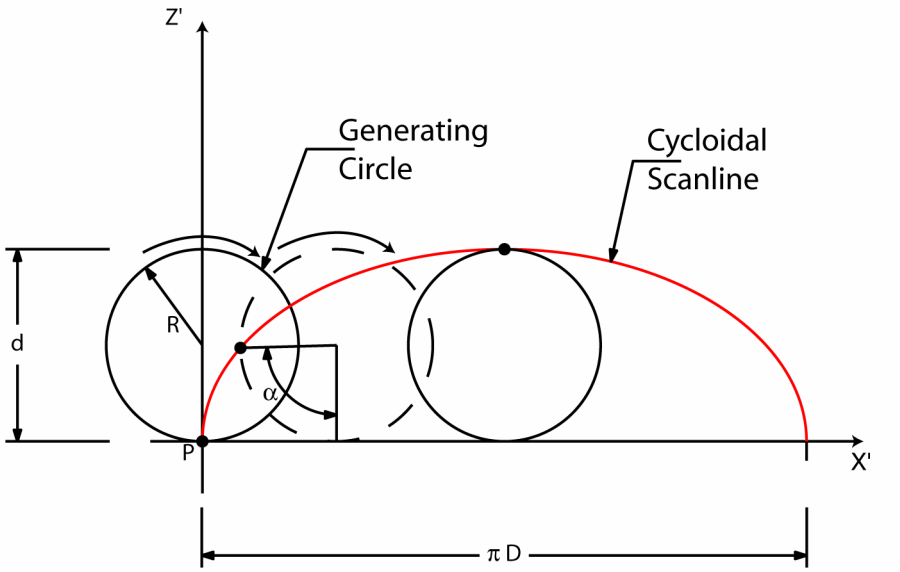


Figure C-1: Generation and dimensions of a cycloidal scanline (red). The generator circle (black circle) is rolled to the right along the line X'. The arc traced out by the point P as the circle rolls creates the cycloid.

For this analysis, scanlines were deployed every ten feet in each of the wells (Figure C-2) and totaled in tables similar to Table C-1 and C-2. The intensities were collected for the entire well, Mesaverde Group as a whole, and also subdivided based upon formation and lithology (Tables C-1 and C-2). The intensities ranged: 0.6 – 1.3 m^{-1} for total Mesaverde Group, 0.07 – 0.86 m^{-1} for the Mesaverde shales, 0.6 - 4.2 m^{-1} for the Mesaverde sandstones (Tables C-1 and C-2). Further intensity measurements are found in Tables C-1 and C-2.

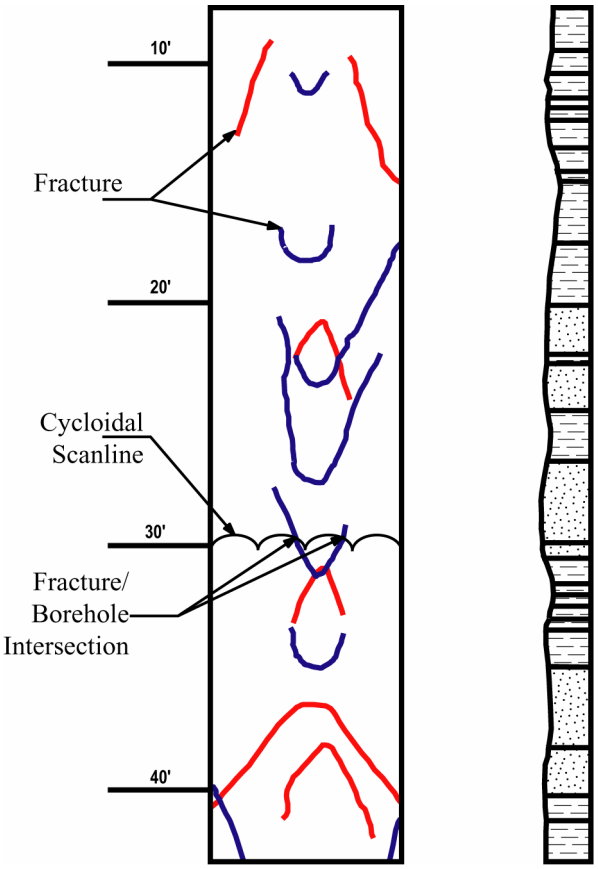


Figure C-2: Cycloidal scanline deployment example. Here, the cycloid is deployed at a depth of 30 feet where it intersects two fracture traces.

Table C-1. Summary of P_{32} estimates by formation for each well

Well	Interval	Number of Intersections	Number of Scanlines	Scanline Length (m)	Scanline Length (ft)	P_{10} (m^{-1})	P_{10} (ft^{-1})	P_{32} (m^2/m^3)	P32 (ft2/ft3)
1	Mesaverde Total	277	524	556.9	1827.1	0.50	0.15	0.99	0.30
	WF Total	195	396	420.9	1380.8	0.46	0.14	0.93	0.28
	Iles Total	62	76	80.8	265.0	0.77	0.23	1.54	0.47
2	Mesaverde Total	201	608	650.5	2134.1	0.31	0.09	0.62	0.19
	WF Total	160	405	433.3	1421.5	0.37	0.11	0.74	0.23
	Iles Total	30	111	118.8	389.6	0.25	0.08	0.51	0.15
3	Mesaverde Total	201	278	300.3	985.1	0.67	0.20	1.34	0.41
	WF Total	156	246	265.7	871.7	0.59	0.18	1.17	0.36
	Iles Total	45	32	34.6	113.4	1.30	0.40	2.60	0.79

Table C-1. Continued

Well	Interval	Number of Intersections	Number of Scanlines	Scanline Length (m)	Scanline Length (ft)	P_{10} (m^{-1})	P_{10} (ft^{-1})	P_{32} (m^2/m^3)	P32 (ft2/ft3)
4	Mesaverde Total	61	145	181.2	594.3	0.34	0.10	0.67	0.21
	WF Total	61	145	181.2	594.3	0.34	0.10	0.67	0.21
5	Mesaverde Total	83	359	393.7	1291.7	0.21	0.06	0.42	0.13
	WF Total	66	304	333.4	1093.8	0.20	0.06	0.40	0.12
	Iles Total	17	55	60.3	197.9	0.28	0.09	0.56	0.17
6	Mesaverde Total	79	447	519.5	1704.3	0.15	0.05	0.30	0.09
	WF Total	68	412	478.8	1570.8	0.14	0.04	0.28	0.09
	Iles Total	11	35	40.7	133.4	0.27	0.08	0.54	0.16

Table C-2. Summary of P_{32} estimates by lithology for each well. Missing lithology indicates lack of data.

Well	Interval	% of Log	Number of Intersections	Number of Scanlines	Scanline Length (m)	Scanline Length (ft)	P_{10} (m^{-1})	P_{10} (ft^{-1})	P_{32} (m^2/m^3)	P_{32} (ft^2/ft^3)
1	WF SS	22.6%	133	111	118.0	387.0	1.13	0.34	2.25	0.69
	WF Shale	45.9%	32	226	240.2	788.0	0.13	0.04	0.27	0.08
2	WF SS	18.8%	95	114	122.0	400.1	0.78	0.24	1.56	0.47
	WF Shale	45.2%	62	275	294.2	965.2	0.21	0.06	0.42	0.13
	Iles SS	6.4%	15	39	41.7	136.9	0.36	0.11	0.72	0.22
	Iles Shale	11.3%	12	69	73.8	242.2	0.16	0.05	0.33	0.10
3	WF SS	6.3%	6	4	4.3	14.2	1.39	0.42	2.78	0.85
	WF Shale	34.9%	4	22	23.8	78.0	0.17	0.05	0.34	0.10
	Iles SS	19.0%	30	12	13.0	42.5	2.31	0.71	4.63	1.41
	Iles Shale	30.2%	15	19	20.5	67.3	0.73	0.22	1.46	0.45

Table C-2. Continued

Well	Interval	% of Log	Number of Intersections	Number of Scanlines	Scanline Length (m)	Scanline Length (ft)	P_{10} (m^{-1})	P_{10} (ft^{-1})	P_{32} (m^2/m^3)	P_{32} (ft^2/ft^3)
4	WF SS	39.3%	31	57	71.2	233.6	0.44	0.13	0.87	0.27
	WF Shale	51.7%	18	75	93.7	307.4	0.19	0.06	0.38	0.12
5	WF SS	18.4%	49	66	72.4	237.5	0.68	0.21	1.35	0.41
	WF Shale	55.7%	8	200	219.3	719.6	0.04	0.01	0.07	0.02
	Iles SS	3.3%	3	12	13.2	43.2	0.23	0.07	0.46	0.14
	Iles Shale	10.3%	7	37	40.6	133.1	0.17	0.05	0.35	0.11
6	WF SS	26.3%	45	127	147.6	484.2	0.30	0.09	0.61	0.19
	WF Shale	53.3%	12	257	298.7	979.9	0.04	0.01	0.08	0.02
	Iles SS	4.8%	11	23	26.7	87.7	0.41	0.13	0.82	0.25
	Iles Shale	2.3%	0	11	12.8	41.9	0.00	0.00	0.00	0.00

VITA

Christopher James Heiny was born in Ft. Walton Beach, Florida on October 8, 1978 to Jerome and Barbara Heiny. He moved to Knoxville, Tennessee at the age of 2 and then to Maryville, Tennessee at 5. In Maryville, he attended Sam Houston Elementary School, Maryville Middle School, and Maryville High School. At Maryville High he was a member of the varsity golf team. After high school, he went to the University of Tennessee, Knoxville where he earned a Bachelor of Science degree in geology in December 2001. He continued his education at the University of Tennessee, Knoxville where he earned a M.S. degree in geology in December 2004. In September 2004, Chris accepted employment as a geologist with the environmental consulting firm Arcadis in Knoxville.